Doctoral Dissertation

Studies on Novel Catalysts Based on Zirconium-Tin Oxide for Direct Decomposition of Nitrous Oxide

（ジルコニウム–スズ複合酸化物を用いた
新規な亜酸化窒素直接分解触媒に関する研究）

HU DONGRUN

January 2024

Department of Applied Chemistry
Graduate School of Engineering
Osaka University

Preface

The study of this doctoral thesis has been conducted under the direct supervision of Professor Dr. Nobuhito Imanaka at Department of Applied Chemistry, Graduate School of Engineering, Osaka University.

The object of the present thesis is to develop novel catalysts based on novel materials of zirconium-tin oxide for direct decomposition of nitrous oxide.

The author desires that the findings and acknowledge obtained in this study will contribute to the further design and development of catalysts for nitrous oxide decomposition and the materials would be widespread application in the future.

HU DONGRUN

Department of Applied Chemistry,
Graduate School of Engineering,
Osaka University,
2-1 Yamadaoka, Suita,
Osaka 565-0871, JAPAN

January 2024

Contents

General Introduction

Nitrous oxide (N_2O) is a well-known environmental pollutant that causes the global warming, and its greenhouse effect is ca. 300 times higher than that of carbon dioxide [1,2]. Also, N_2O is a stratospheric ozone-depleting gas, similar to chlorofluorocarbons [3]. Since N_2O is emitted by manufacturing processes, such as production of adipic acid and nitric acid, recent development of industry causes the increase of N_2O concentration in the atmosphere [4,5]. In order to prevent global warming as well as ozone layer depletion, it is important to decompose N_2O from industrial exhaust gases.

Several methods for N_2O decomposition have been reported, including selective catalytic reduction (SCR) [6-8], thermal decomposition [9], and direct catalytic decomposition [10-35]. In the SCR method, N_2O is reduced by a reducing agent, such as NH_3, into nontoxic N_2 and H_2O over SCR catalysts. However, a continuous supply of the reducing additive is required. Since NH_3 has toxicity, corrosiveness, and flammability, the control system for safety is indispensable. For thermal decomposition, N_2O is decomposed into nontoxic N_2 and O_2 by applying elevated temperatures over 800 °C. Although the decomposition can proceed without using reducing agents, the high temperatures cause heat deterioration in the system and require significant energy consumption. In contrast, direct catalytic decomposition of N_2O into N_2 and O_2 is considered to be a promising method, because there is no need for reducing agents and the required temperature is moderate compared to the case of thermal decomposition.

According to previous studies, various catalysts for direct N_2O decomposition have been studied. It is known that Rh based catalysts are effective to decompose N_2O [10-17], as listed in **Table G-1**. In the Rh based systems, high catalytic activities have been reported for the catalysts having high specific surface areas, such as 2 wt% Rh/USY (complete decomposition: 250 °C, specific surface area: 695 $m^2 \cdot g^{-1}$). However, the morphology of the support material is strictly controlled, because a decrease in the specific surface area generally induces the deactivation owing to a decrease in the number of active sites, caused by a Rh aggregation. The reported catalysts having low specific surface areas show low activities even with noble metals, such as 1 wt% Rh/ZrO_2 (complete decomposition: 550 °C, specific surface area: 79 $m^2 \cdot g^{-1}$). For noble-metal-free catalysts, spinel-type oxides [18-21], perovskite-type oxides [22-25], hexaaluminates [26-29], and zeolites [30-33] have been reported,

Table G-1. Reported Rh based catalysts for N_2O decomposition

Catalyst	Complete decomposition temperature / °C	Specific surface area / $m^2 \cdot g^{-1}$	Reaction condition	Ref.
2 wt% Rh/USY [a]	250	695	0.095% N_2O/He, 60000 $mL \cdot g^{-1} \cdot h^{-1}$	[10]
2 wt% Rh/Al_2O_3	300	168	0.095% N_2O/He, 60000 $mL \cdot g^{-1} \cdot h^{-1}$	[10]
2 wt% Rh/Mg/Al	400	289	0.1% N_2O/N_2, 480000 $mL \cdot g^{-1} \cdot h^{-1}$	[11]
1 wt% $Rh/Ag/Al_2O_3$	400	138	0.1% N_2O/He, 300000 $mL \cdot g^{-1} \cdot h^{-1}$	[12]
1 wt% Rh/KIT-6 [b]	420	602	0.17% N_2O/He, 120000 $mL \cdot g^{-1} \cdot h^{-1}$	[13]
1wt%Rh/Al_2O_3	550	110	1% N_2O/He, 1800 $mL \cdot g^{-1} \cdot h^{-1}$	[14]
1wt%Rh/ZrO_2	550	79	1% N_2O/He, 1800 $mL \cdot g^{-1} \cdot h^{-1}$	[14]

[a] USY: Ultrastable Y zeolite, [b] KIT-6: Korea Advanced Institute of Science and Technology No. 6

Table G-2. Typical noble-metal-free catalysts for N_2O decomposition

Catalyst	Complete decomposition temperature / °C	Specific surface area / $m^2 \cdot g^{-1}$	Reaction condition	Ref.
Co_3O_4 (Spinel-type oxide)	500	29	0.1% N_2O/He, 20000 $mL \cdot g^{-1} \cdot h^{-1}$	[21]
$LaCoO_3$ (Perovskite-type oxide)	550	8	0.5% N_2O/He, 120000 $mL \cdot g^{-1} \cdot h^{-1}$	[22]
$LaFeAl_{11}O_{19}$ (Hexaaluminate)	825	11	0.15% N_2O/He, 60000 $mL \cdot g^{-1} \cdot h^{-1}$	[29]
Co-clinoptilolite (Zeolite)	550	27	0.04% N_2O/N_2, 4500 $mL \cdot g^{-1} \cdot h^{-1}$	[30]

where typical catalysts are tabulated in **Table G-2**. Although their activities are lower than those of the Rh based catalysts having high specific surface areas, the spinel-type Co_3O_4 catalyst has effective N_2O decomposition ability compared to the other metal oxides.

The reaction mechanism for N_2O decomposition has been suggested as follows [34,35]: N_2O molecules are adsorbed on the catalytically active sites ([cat]) (**Eq. G-1**), decomposition of adsorbed N_2O into gaseous N_2 and adsorbed oxygen (**Eq. G-2**), and reaction of adsorbed oxygen with gaseous N_2O (**Eq. G-3**) or combination of two adsorbed oxygen species (**Eq. G-4**).

$$N_2O + [cat] \rightarrow N_2O\text{-}[cat] \qquad \textbf{(Eq. G-1)}$$

$$N_2O\text{-}[cat] \rightarrow N_2 + O\text{-}[cat] \qquad \textbf{(Eq. G-2)}$$

$$O\text{-}[cat] + N_2O \rightarrow [cat] + N_2 + O_2 \qquad \textbf{(Eq. G-3)}$$

$$2\ O\text{-}[cat] \rightarrow 2\ [cat] + O_2 \qquad \textbf{(Eq. G-4)}$$

In the above reaction mechanism, the regeneration of the catalytically active sites via removing adsorbed oxygen (**Eqs. G-3 and G-4**) is known to be the rate-determining step [34,35]. One effective

method to facilitate the removal of residual oxygen species is the introduction of promoters with the ability to supply oxygen species from inside the lattice. The proposed reaction is as follows: reaction of the adsorbed oxygen species and an oxide ion in the promoter to form gaseous O_2 with the generation of oxygen vacancies (V_O) and the reduction of M^{n+} (cation in the promoter):

$$O\text{-}[cat] + O^{2-} + 2\,M^{n+} \rightarrow [cat] + O_2 + V_O + 2\,M^{(n-1)+} \qquad \textbf{(Eq. G-5)}$$

Oxygen vacancies and electrons migrate through the lattice, and they are compensated by oxygen species adsorbed on another active site ([cat]'):

$$V_O + 2\,M^{(n-1)+} + O\text{-}[cat]' \rightarrow O^{2-} + 2\,M^{n+} + [cat]' \qquad \textbf{(Eq. G-6)}$$

Based on the mechanism, the oxygen supply ability of the promoter should be related to the redox properties and the oxide ion conducting property.

In the Imanaka laboratory, to which I belong, single-phase zirconium-tin oxide ($ZrSnO_4$) with an α-PbO_2-type structure was firstly synthesized, and its crystal structure was demonstrated with Rietveld analysis (**Figure G-1**) [36]. This material may have redox properties because of the valence change between Sn^{4+} and Sn^{2+}. In addition, the coexistence of Sn^{2+} can generate oxygen vacancies for oxide ion migration. Therefore, $ZrSnO_4$ is expected to have the oxygen supply ability. In this doctoral dissertation, $ZrSnO_4$ was focused to develop novel catalysts for direct decomposition of N_2O.

This thesis consists of the following three chapters.

Chapter 1 aims to develop novel catalysts with high catalytic activity by selecting $ZrSnO_4$ as a promoter. By combining the $ZrSnO_4$ promoter and a Rh activator having N_2O decomposition ability, Rh/$ZrSnO_4$ catalysts were prepared, and their N_2O direct decomposition activities were investigated.

In **Chapter 2**, in order to develop the catalysts without using noble metals, Co_3O_4 was selected as an activator instead of Rh. In addition, to obtain the high catalytic activity, $Fe^{2+/3+}$ ions were introduced into $ZrSnO_4$, becasue the valence changes of $Fe^{2+/3+}$ may improve the redox properties and the replacement of Sn^{4+} for lower-valent $Fe^{2+/3+}$ can generate oxygen vacancies for smooth oxide ion migration. Therefore, $Co_3O_4/ZrSn_{1-x}Fe_xO_{4-\delta}$ catalysts were prepared, and the catalytic activities for N_2O direct decomposition were investigated.

Chapter 3 deals with the catalysts with durability against coexisting gases of oxygen gas and water vapor. To this end, $Co^{2+/3+}$ doping was carried out into the $ZrSnO_4$ lattice, instead of $Co^{2+/3+}$ loading as Co_3O_4. The introduction of $Co^{2+/3+}$ was expected to improve the redox properties due to two types of valence states (Co^{2+} and Co^{3+}) and to generate oxygen vacancies caused by the lower-valence states of $Co^{2+/3+}$ than that of Sn^{4+}. Therefore, $ZrSn_{1-x}Co_xO_{4-\delta}$ solids were prepared, and their N_2O direct decomposition activities were investigated.

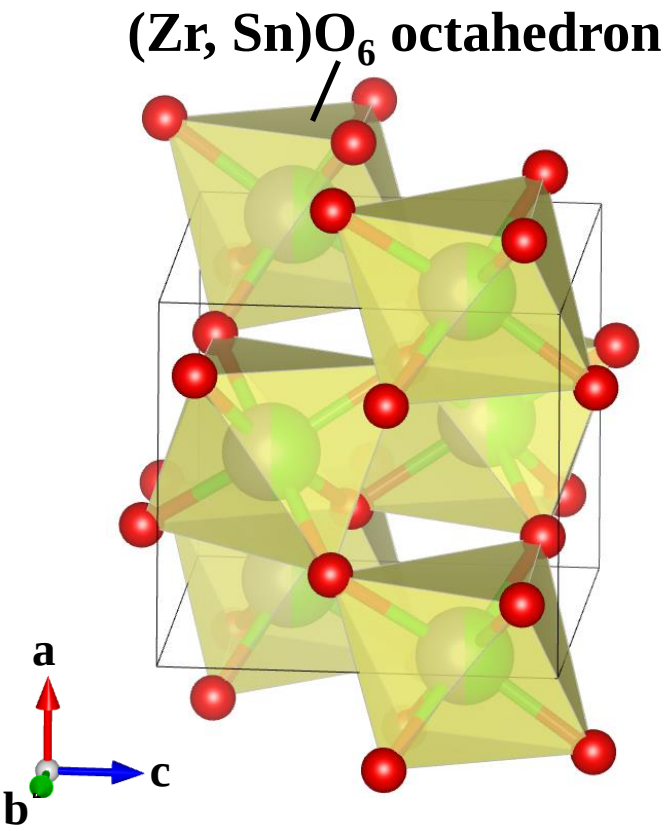

Figure G-1. Crystal structure of $ZrSnO_4$ [36].

List of Publications

1. Direct Decomposition of Nitrous Oxide by Rhodium Supported on $ZrSnO_4$

   Dong-Run Hu, Naoyoshi Nunotani, and Nobuhito Imanaka*

   Functional Materials Letters, **2023**, *16 (3&4)*, 2350016:1–4.

2. Direct Decomposition of N_2O over $Co_3O_4/ZrSn_{1-x}Fe_xO_{4-\delta}$ Catalysts

   Dong-Run Hu, Naoyoshi Nunotani, and Nobuhito Imanaka*

   Functional Materials Letters, **2023**, *16 (6)*, 2350023:1–4.

3. Novel Cobalt-doped $ZrSnO_4$ Catalysts for Direct Nitrous Oxide Decomposition

   Dong-Run Hu, Naoyoshi Nunotani, and Nobuhito Imanaka*

   International Journal of Applied Ceramic Technology, **2023**, *20 (2)*, 966–971.

Chapter 1

Novel Catalysts of Rh/$ZrSnO_4$ for Direct Decomposition of N_2O

1.1. Introduction

As described in the General Introduction section, the promoter which can supply oxygen species from inside the lattice may facilitate N_2O decomposition. In addition, $ZrSnO_4$ is expected to have oxygen supply ability due to its redox properties through the valence change between Sn^{4+} and Sn^{2+} and oxygen vacancies for oxide ion migration formed by the coexistence of Sn^{2+}.

In Chapter 1, in order to develop novel catalysts with high catalytic activity, the $ZrSnO_4$ solid was selected as a promoter, and a Rh activator having N_2O decomposition ability was loaded onto $ZrSnO_4$. Therefore, Rh/$ZrSnO_4$ catalysts were prepared, and their catalytic activities for N_2O decomposition were investigated.

1.2. Experimental Procedure

The $ZrSnO_4$ solid was prepared using a co-precipitation method as follows. Powders of zirconium (IV) oxynitrate dihydrate ($ZrO(NO_3)_2 \cdot 2H_2O$, Kishida Chemical, ≥ 99.0%) (0.4864 g) and tin (II) oxalate (SnC_2O_4, Sigma-Aldrich, 99%) (0.2891 g) were weighed, where a Zr:Sn ratio was 1.3:1. They were added into deionized water, and then nitric acid solution (Kishida Chemical, 60%) (10 mL) was poured into the mixture to obtain a homogenous solution, followed by stirring at room

temperature for 30 min. Subsequently, the pH was adjusted to 11 by dropwise addition of an aqueous ammonia solution (Kishida Chemical, 28%). After stirring for 6 h at room temperature, the resulting precipitate was collected by filtration, washed with deionized water, and then dried at 80 °C for 6 h. Finally, the powder was calcined at 600 °C for 1 h under air flow (10 $mL \cdot min^{-1}$).

Rh supported on catalysts were prepared via impregnating the $ZrSnO_4$ powders (0.3000 g) with 0.01 $mol \cdot L^{-1}$ $RhCl_3$ aqueous solution (prepared by dissolving rhodium (III) chloride hydrate ($RhCl_3 \cdot nH_2O$, Kishida Chemical) in deionized water). After the evaporation of the solvent at 180 °C using a hot stirrer, the residue was ground by using an agate mortar, followed by the calcination at 500 °C for 2 h in the air to obtain x wt% $Rh/ZrSnO_4$ (x = 0.5, 1.0, 1.5, and 2.0). For comparison purpose, 1.0 wt% Rh/SnO_2, 1.0 wt% Rh/ZrO_2, and 1.0 wt% Rh/Al_2O_3 were prepared by a similar impregnation method using tin (IV) oxide (SnO_2, Kojundo Chemical Laboratory, ≥ 99.9%), zirconium (IV) oxide (ZrO_2, Kanto Chemical, ≥ 99.9%) and aluminum (III) oxide (Al_2O_3, Kojundo Chemical Laboratory, ≥ 99.99%).

The crystal structures were identified by using X-ray powder diffraction (XRD; SmartLab, Rigaku) with Cu Kα radiation (40 kV and 30 mA) in the 2θ range between 10 and 70 deg. The XRD data were analyzed by whole powder pattern fitting using PDXL software (Rigaku) to calculate the crystallite size. The Rh loading amount and sample compositions were determined by X-ray fluorescence spectroscopy (XRF; Supermini200, Rigaku) analysis. The Brunauer–Emmett–Teller (BET) specific surface area was determined at −196 °C in a nitrogen environment (Micromeritics TriStar 3000 analyzer, Shimadzu). The Rh dispersion was determined using a CO-pulse method at

50 °C with 10 vol% CO - 90 vol% He (0.03 mL) over 0.05 g of the catalyst, under the suppose that one CO molecule adsorbs to one surface Rh atom (BELCAT-B, MicrotracBEL). After preheating at 200 °C for 1 h under a helium flow (50 $mL \cdot min^{-1}$), hydrogen temperature-programmed reduction (TPR) measurement was carried out under a reducing gas flow (5 vol% H_2 - 95 vol% Ar at 50 $mL \cdot min^{-1}$) at a heating rate of 5 $°C \cdot min^{-1}$ over 0.05 g of the sample (BELCAT-B, MicrotracBEL). The valence sate of surfaces Rh species was investigated by X-ray photoelectron spectroscopy (XPS; PHI5000 VersaProbe II, ULVAC-PHI) with Al Kα radiation, and the effect of charging on the binding energies was refined by the C 1s peak (284.6 eV), and the spectrum was fitted using a Shirley background and Gaussian–Lorentzian line shapes.

The catalytic activity for N_2O direct decomposition was investigated using a conventional fixed-bed flow reactor with a silica-glass tube (10 mm diameter). **Figure 1-1** illustrates a schematic view of the fixed-bed flow reactor for the N_2O direct decomposition. The reactant gas of 0.5 vol% N_2O - 99.5 vol% He was fed at 60 $mL \cdot min^{-1}$ over 0.2 g of the catalyst with a catalyst weight hourly space velocity of 18,000 $mL \cdot g^{-1} \cdot h^{-1}$. Before the catalytic activity tests, each catalyst was preheated at 200 °C for 1 h under a helium flow (50 $mL \cdot min^{-1}$). After the catalytic reaction, the N_2O conversion was determined using a gas chromatograph equipped with a thermal conductivity detector (GC-8AIT, Shimadzu).

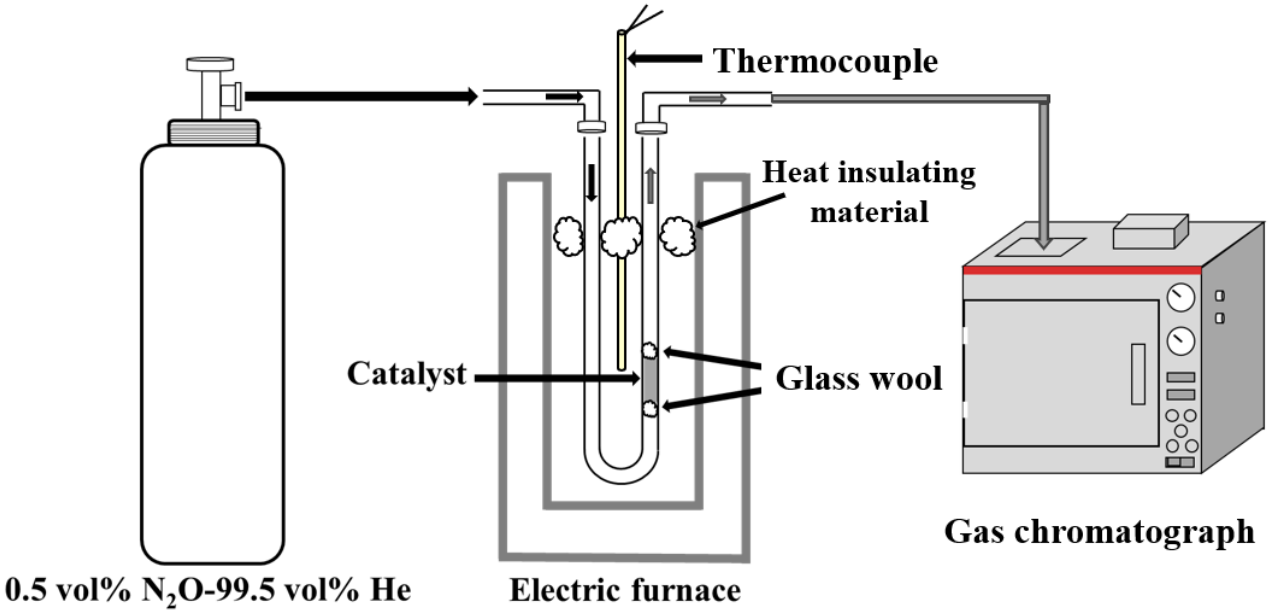

Figure 1-1. A schematic view of the fixed-bed flow reactor for N_2O direct decomposition.

1.3. Results and Discussion

Figure 1-2 shows the XRD patterns of the *x* wt% Rh/$ZrSnO_4$ (*x* = 0.5, 1.0, 1.5, 2.0) catalysts with the data of $ZrSnO_4$. The $ZrSnO_4$ solid exhibited the single-phase of the α-PbO_2-type structure. For the *x* wt% Rh/$ZrSnO_4$ catalysts, peaks were identified as only the α-PbO_2-type phase, and no peak related to the Rh species was detected. This was probably due to the low loading amount of Rh.

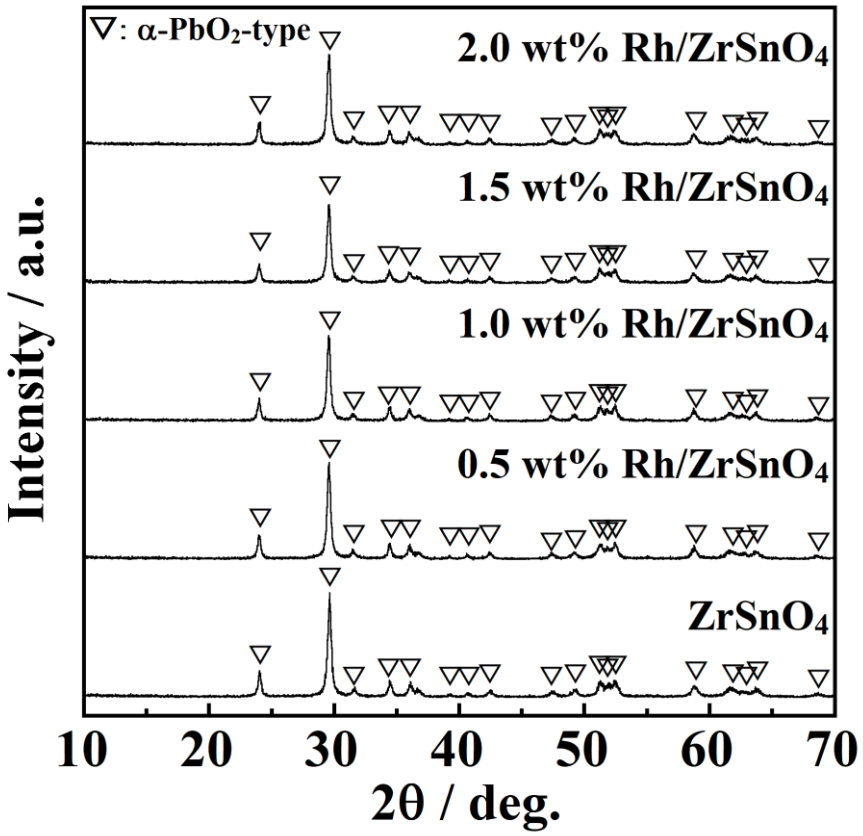

Figure 1-2. XRD patterns of *x* wt% Rh/$ZrSnO_4$ and $ZrSnO_4$.

The measured composition, specific surface area, crystallite size of $ZrSnO_4$, and Rh dispersion of the *x* wt% Rh/$ZrSnO_4$ catalysts are summarized in **Table 1-1**. The measured compositions were in good agreement with the feed values within the experimental error; that is, Rh was successfully loaded onto the $ZrSnO_4$ solid. For the specific surface area, all the samples showed similar values of ca. 13 $m^2 \cdot g^{-1}$. Furthermore, similar crystallite sizes of $ZrSnO_4$ (ca. 32 nm) were obtained. These results might be explained by the fact that $ZrSnO_4$ was prepared by the same method before loading Rh. In contrast, the Rh dispersion decreased monotonously with increasing the Rh loading amount (*x*), suggesting the Rh aggregation on the $ZrSnO_4$ surface.

Table 1-1. Measured composition, specific surface area, crystallite size of $ZrSnO_4$, and Rh dispersion of the *x* wt% Rh/$ZrSnO_4$ catalysts

Feed composition	Measured composition	Specific surface area / $m^2 \cdot g^{-1}$	Crystallite size of $ZrSnO_4$ / nm	Rh dispersion / %
$ZrSnO_4$	$Zr_{1.07}Sn_{0.93}O_4$	14.0	33	-
0.5 wt% Rh/$ZrSnO_4$	0.52 wt% Rh/$Zr_{1.07}Sn_{0.93}O_4$	13.0	32	53.2
1.0 wt% Rh/$ZrSnO_4$	0.96 wt% Rh/$Zr_{1.08}Sn_{0.92}O_4$	13.6	33	32.8
1.5 wt% Rh/$ZrSnO_4$	1.56 wt% Rh/$Zr_{1.03}Sn_{0.97}O_4$	12.0	31	24.8
2.0 wt% Rh/$ZrSnO_4$	2.00 wt% Rh/$Zr_{1.06}Sn_{0.94}O_4$	12.0	30	21.3

In order to investigate the oxidation states of the surface Rh species, XPS measurements were performed for the *x* wt% Rh/$ZrSnO_4$ catalysts. **Figure 1-3** presents the XPS results of the Rh 3d core levels, where the fitting parameters are tabulated in **Table 1-2**. For all the samples, the $Rh_{3/2}$ and $Rh_{5/2}$ peaks could be divided into Rh^{3+} and $Rh^{(0)}$ peaks. The ratios of $Rh^{3+}/(Rh^{3+}+Rh^{(0)})$ were calculated by the peak areas related to Rh^{3+} and $Rh^{(0)}$ in the XPS spectra, and the results are listed in **Table 1-3**. The $Rh^{3+}/(Rh^{3+}+Rh^{(0)})$ ratios for all the samples were almost the same values (ca. 81%), irrespective of the Rh loading amount.

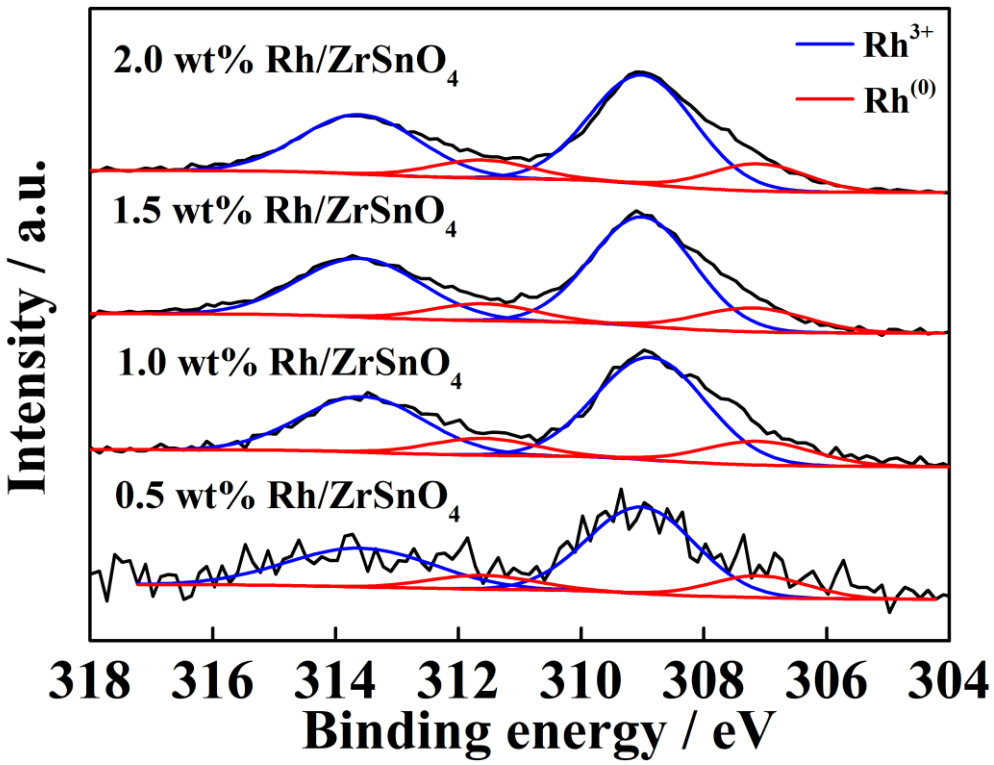

Figure 1-3. XPS spectra of the Rh 3d core levels of the *x* wt% Rh/$ZrSnO_4$ catalysts.

Table 1-2. Fitting parameters of of the Rh 3d XPS spectra for *x* wt% $Rh/ZrSnO_4$

Catalyst	χ^2	Peak	Position / eV	FWHM / eV	Area / %
0.5 wt% $Rh/ZrSnO_4$	0.294	Rh^{3+} $3d_{5/2}$	309.0	2.1	15.0
		Rh^{3+} $3d_{3/2}$	313.6	2.8	9.2
		$Rh^{(0)}$ $3d_{5/2}$	307.1	1.9	3.4
		$Rh^{(0)}$ $3d_{3/2}$	311.6	2.0	2.4
1.0 wt% $Rh/ZrSnO_4$	0.037	Rh^{3+} $3d_{5/2}$	308.9	2.1	18.1
		Rh^{3+} $3d_{3/2}$	313.6	2.4	11.0
		$Rh^{(0)}$ $3d_{5/2}$	307.1	2.1	4.1
		$Rh^{(0)}$ $3d_{3/2}$	311.6	2.0	2.9
1.5 wt% $Rh/ZrSnO_4$	0.027	Rh^{3+} $3d_{5/2}$	309.0	2.0	18.0
		Rh^{3+} $3d_{3/2}$	313.6	2.3	11.6
		$Rh^{(0)}$ $3d_{5/2}$	307.2	2.1	4.2
		$Rh^{(0)}$ $3d_{3/2}$	311.6	2.0	2.9
2.0 wt% $Rh/ZrSnO_4$	0.018	Rh^{3+} $3d_{5/2}$	309.0	2.0	18.3
		Rh^{3+} $3d_{3/2}$	313.6	2.3	11.3
		$Rh^{(0)}$ $3d_{5/2}$	307.1	1.8	4.2
		$Rh^{(0)}$ $3d_{3/2}$	311.6	1.9	2.9

Table 1-3. Ratio of $Rh^{3+}/(Rh^{3+}+Rh^{(0)})$ for *x* wt% $Rh/ZrSnO_4$

Catalyst	$Rh^{3+}/(Rh^{3+}+Rh^{(0)})$
0.5 wt% $Rh/ZrSnO_4$	81.5 %
1.0 wt% $Rh/ZrSnO_4$	81.5 %
1.5 wt% $Rh/ZrSnO_4$	81.1 %
2.0 wt% $Rh/ZrSnO_4$	81.3 %

Figure 1-4 displays the temperature dependence of the N_2O conversion for the *x* wt% $Rh/ZrSnO_4$ catalysts. While the $ZrSnO_4$ solid showed the low activity, the loading of the Rh activator drastically increased the catalytic activity. For the catalysts with $x \leq 1.0$, with increasing the Rh loading amount (*x*), the catalytic activity improved up to $x = 1.0$. This phenomenon can be explained by the increase in the Rh loading amount. In contrast, the decrease in the catalytic activity was observed for the catalysts with $x > 1.0$, likely due to the decrease in the Rh dispersion. In order to determine the effect of the Rh dispersion, the turnover frequency (TOF) values per mole of Rh at 400 °C were estimated, and the results are listed in **Table 1-4**. The TOF values decreased monotonously with increasing *x*. This trend is similar to that of the Rh dispersions (**Table 1-1**). The increase in the activity at $x \leq 1.0$ was only affected by the amount of Rh loading, whereas the catalytic activity at $x > 1.0$ decreased by the decrease in the number of active sites due to the Rh aggregation. Among the prepared catalysts, the highest activity was obtained for the 1.0 wt% $Rh/ZrSnO_4$ catalyst, and the complete N_2O decomposition was achieved at 450 °C.

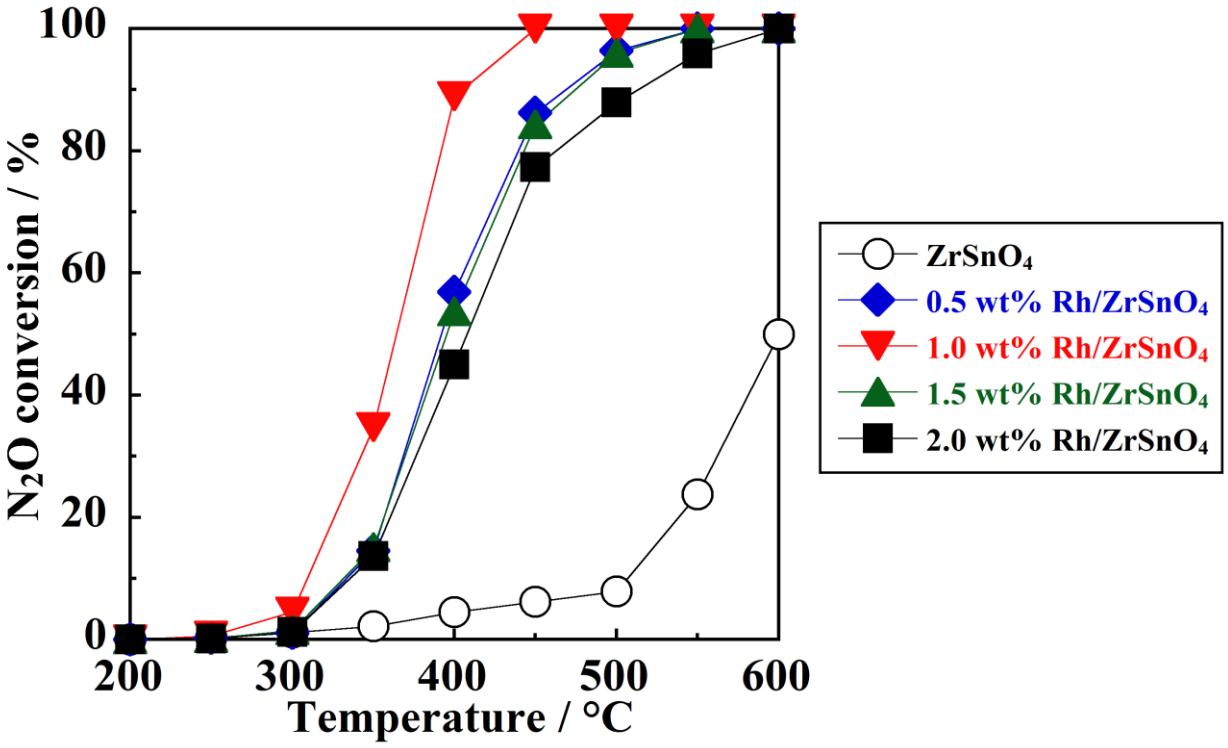

Figure 1-4. Temperature dependence of the N_2O conversion for the *x* wt% $Rh/ZrSnO_4$ catalysts.

Table 1-4. TOF values per mole of Rh for the *x* wt% $Rh/ZrSnO_4$ catalysts at 400 °C

Catalyst	TOF (10^{-3} s^{-1})
0.5 wt% $Rh/ZrSnO_4$	12.0
1.0 wt% $Rh/ZrSnO_4$	9.4
1.5 wt% $Rh/ZrSnO_4$	3.8
2.0 wt% $Rh/ZrSnO_4$	2.4

In order to investigate the effect of $ZrSnO_4$ on the catalytic activity, 1.0 wt% Rh/SnO_2, 1.0 wt% Rh/ZrO_2 and 1.0 wt% Rh/Al_2O_3 catalysts were prepared as the comparison. **Figure 1-5** shows the XRD patterns of 1.0 wt% Rh/SnO_2, 1.0 wt% Rh/ZrO_2, and 1.0 wt% Rh/Al_2O_3, with the data of 1.0 wt% Rh/$ZrSnO_4$. For each sample, no peaks related to impurities and the Rh species were detected. The specific surface areas of 1.0 wt% Rh/SnO_2, 1.0 wt% Rh/ZrO_2, and 1.0 wt% Rh/Al_2O_3 were measured to be 6.9 $m^2 \cdot g^{-1}$, 13.0 $m^2 \cdot g^{-1}$, and 5.8 $m^2 \cdot g^{-1}$, respectively.

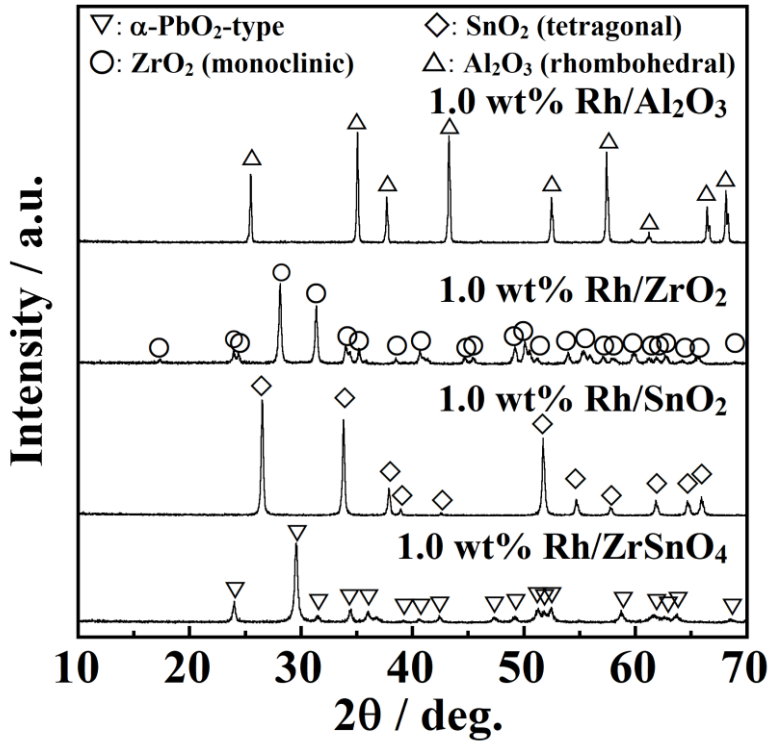

Figure 1-5. XRD patterns of the 1.0 wt% Rh/$ZrSnO_4$, 1.0 wt% Rh/SnO_2, 1.0 wt% Rh/ZrO_2, and 1.0 wt% Rh/Al_2O_3 catalysts.

Figure 1-6 presents the TPR profiles of the $ZrSnO_4$, SnO_2, ZrO_2, and Al_2O_3 solids. For ZrO_2, and Al_2O_3 solids, there were no obvious reduction peaks below 500 °C. In the cases of $ZrSnO_4$ and SnO_2, the shoulder peak was observed at the temperatures higher than 300 °C, likely because of the reduction of Sn^{4+}. The onset reduction temperature for $ZrSnO_4$ was 310 °C, which is lower than that for SnO_2 (375 °C). Therefore, $ZrSnO_4$ can release oxygen species from inside the lattice, and its ability is higher than those for SnO_2, ZrO_2, and Al_2O_3.

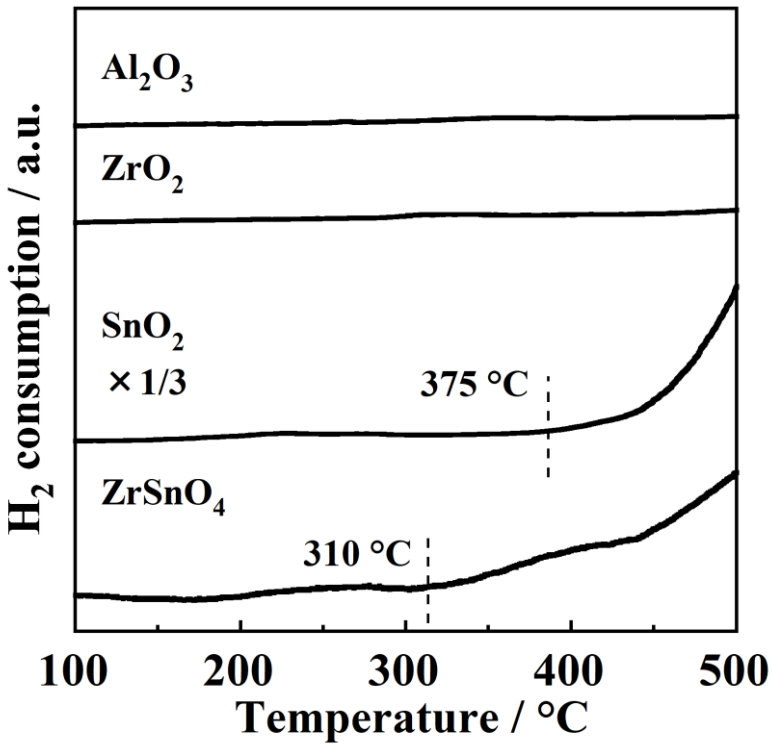

Figure 1-6. TPR profiles of the $ZrSnO_4$, SnO_2, ZrO_2, and Al_2O_3 solids.

Figure 1-7 shows the temperature dependence of the N_2O conversion for the 1.0 wt% $Rh/ZrSnO_4$, 1.0 wt% Rh/SnO_2, 1.0 wt% Rh/ZrO_2, and 1.0 wt% Rh/Al_2O_3 catalysts. Regardless of the same Rh loading amount and similar low specific surface areas (1.0 wt% $Rh/ZrSnO_4$: 13.6 $m^2 \cdot g^{-1}$, 1.0 wt% Rh/SnO_2: 6.9 $m^2 \cdot g^{-1}$, 1.0 wt% Rh/ZrO_2: 13.0 $m^2 \cdot g^{-1}$, 1.0 wt% Rh/Al_2O_3: 5.8 $m^2 \cdot g^{-1}$), the catalytic activity of 1.0 wt% $Rh/ZrSnO_4$ was significantly higher than those of 1.0 wt% Rh/SnO_2, 1.0 wt% Rh/ZrO_2, and 1.0 wt% Rh/Al_2O_3. The highest oxygen release ability of $ZrSnO_4$ might contribute to the highest catalytic activity. Here, the activity of 1.0 wt% Rh/SnO_2 was higher than those of 1.0 wt% Rh/ZrO_2 and 1.0 wt% Rh/Al_2O_3, because of the oxygen release from the SnO_2 lattice. Therefore, the $ZrSnO_4$ solid effectively promoted the N_2O decomposition over Rh, because the oxygen supply from inside the $ZrSnO_4$ lattice toward the Rh activator might remove adsorbed oxygen species which were generated on Rh during the N_2O decomposition process.

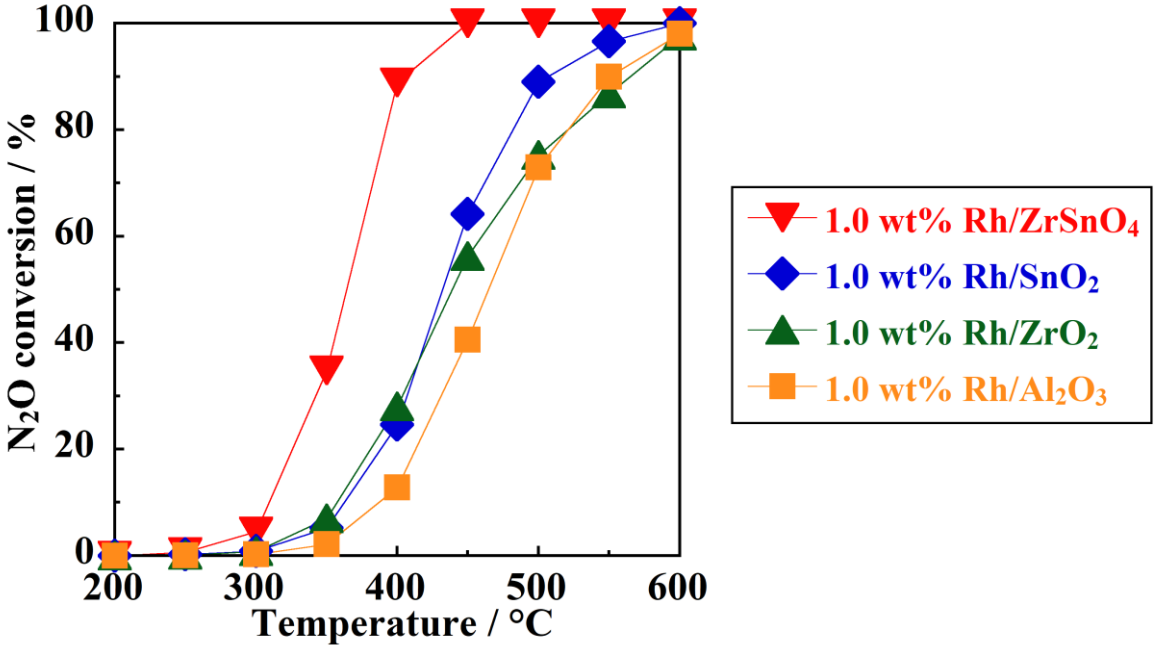

Figure 1-7. Temperature dependence of the N_2O conversion for the 1.0 wt% $Rh/ZrSnO_4$, 1.0 wt% Rh/SnO_2, 1.0 wt% Rh/ZrO_2, and 1.0 wt% Rh/Al_2O_3 catalysts.

1.4. Conclusion

In this chapter, in order to develop novel catalysts for N_2O decomposition, Rh supported on $ZrSnO_4$ were synthesized. Among the prepared catalysts, the 1.0 wt% Rh/$ZrSnO_4$ catalyst exhibited the highest activity, and N_2O was completely decomposed at 450 °C. In addition, Rh/$ZrSnO_4$ exhibited the higher catalytic activity than those of Rh/SnO_2, Rh/ZrO_2, and Rh/Al_2O_3, suggesting that the oxygen supply from the $ZrSnO_4$ lattice could facilitate the removal of adsorbed surface oxygen, generated on the Rh activator during the N_2O decomposition process.

Chapter 2

Noble-metal-free Catalysts Based on $ZrSnO_4$ for Direct Decomposition of N_2O

2.1. Introduction

Chapter 1 demonstrated that $ZrSnO_4$ could promote N_2O decomposition over the Rh activator, and 1.0 wt% $Rh/ZrSnO_4$ completely decomposed N_2O at 450 °C. However, owing to the high cost and scarce resources of noble metals, noble-metal-free catalysts are desired for the widespread industrial applications.

This chapter aims the development of novel noble-metal-free catalysts with high activity. To this end, Co_3O_4 was selected as an activator instead of Rh, because spinel-type Co_3O_4 based catalysts are known to be effective for N_2O decomposition, described in the General Introduction section. Furthermore, in order to increase the oxygen supply ability of $ZrSnO_4$, $Fe^{2+/3+}$ ions were introduced into $ZrSnO_4$, where the valence change of $Fe^{2+/3+}$ may improve the redox properties and the replacement of the Sn^{4+} site for lower-valent $Fe^{2+/3+}$ can generate oxygen vacancies for smooth oxide ion migration. Therefore, noble-metal-free catalysts of $Co_3O_4/ZrSn_{1-x}Fe_xO_{4-\delta}$ were synthesized, and the activities for N_2O direct decomposition were investigated.

2.2. Experimental Procedure

The $ZrSn_{1-x}Fe_xO_{4-\delta}$ powders were prepared by a co-precipitation method by using starting

materials of zirconium (IV) oxynitrate dihydrate ($ZrO(NO_3)_2 \cdot 2H_2O$, Kishida Chemical, ≥ 99.0%), tin (II) oxalate (SnC_2O_4, Sigma-Aldrich, 99%), and 0.5 $mol \cdot L^{-1}$ $Fe(NO_3)_3$ aqueous solution (prepared by dissolving iron (III) nitrate nonahydrate ($Fe(NO_3)_3 \cdot 9H_2O$, FUJIFILM Wako Pure Chemical, 99.9%) in deionized water) according to a Zr:Sn:Fe molar ratio of 1.3:(1−*x*):*x*. The subsequent experimental methods are the same as described in Chapter 1.

The Co_3O_4 loading was conducted by impregnating the $ZrSn_{1-x}Fe_xO_{4-\delta}$ powders with cobalt (II) nitrate hexahydrate ($Co(NO_3)_2 \cdot 6H_2O$, Kishida Chemical, ≥ 98.0%) in 40 mL of deionized water. The 1.1 molar equivalents to Co ions of citric acid (FUJIFILM Wako Pure Chemical, 98.0%) and 5.0 molar equivalents to Co ions of 1,2-propanediol (Kishida Chemical, ≥ 99.0%) were added as dispersants. After the mixture was stirred at 90 °C for 4 h, the solvent was evaporated at 150 °C. Subsequently, the resulting solid was pulverized, and then calcinated at 600 °C for 1 h in the air. The Co_3O_4 loading amount was adjusted to be *y* wt% (*y* = 11, 18, 19, 20, and 27). In particular, 19 wt% $Co_3O_4/ZrSn_{1-x}Fe_xO_{4-\delta}$ were denoted as $Co_3O_4/ZrSn_{1-x}Fe_xO_{4-\delta}$.

The obtained sample compositions were determined by using XRF (Supermini200, Rigaku). The BET specific surface area was determined by using a Micromeritics TriStar 3000 analyzer (Shimadzu). The crystal structures were identified through XRD (SmartLab, Rigaku) with Cu Kα radiation, where the lattice volumes were calculated through refining the XRD peak angles using α-alumina as the internal standard. TPR measurements were conducted as described in Chapter 1. The catalytic activity for N_2O direct decomposition was also carried out according to Chapter 1.

2.3. Results and Discussion

The XRD patterns of the $ZrSn_{1-x}Fe_xO_{4-\delta}$ (x = 0.03, 0.05, 0.07, 0.10) solids are presented in **Figure 2-1**. All the samples showed a single-phase of the α-PbO_2-type structure, where no crystalline phases were detected. The lattice volumes of $ZrSn_{1-x}Fe_xO_{4-\delta}$ were estimated using the XRD patterns, and the compositional dependence of the lattice volume is depicted in **Figure 2-2**. With increasing the $Fe^{2+/3+}$ content (x), the lattice volume decreased monotonously until x = 0.07, indicating that the Sn^{4+} (Sn^{4+}: 0.083 nm, coordination number [CN] = 6) site in $ZrSnO_4$ was partially replaced for the smaller $Fe^{2+/3+}$ ions (Fe^{2+}: 0.075 nm, Fe^{3+}: 0.069 nm, CN = 6) [37]. Here, since the valence states of $Fe^{2+/3+}$ are lower than that of Sn^{4+}, oxygen vacancies shoud be formed in the lattice by the charge compensation mechanism. For the sample with x = 0.10, no significant lattice volume change was observed compared to the sample with x = 0.07. Since the x = 0.10 sample showed only the peaks corresponding to the α-PbO_2-type phase from the XRD pattern, an excess Fe component might exist as an amorphous phase. Therefore, the solid solubility limit composition is considered to be $ZrSn_{0.93}Fe_{0.07}O_{4-\delta}$ (x = 0.07).

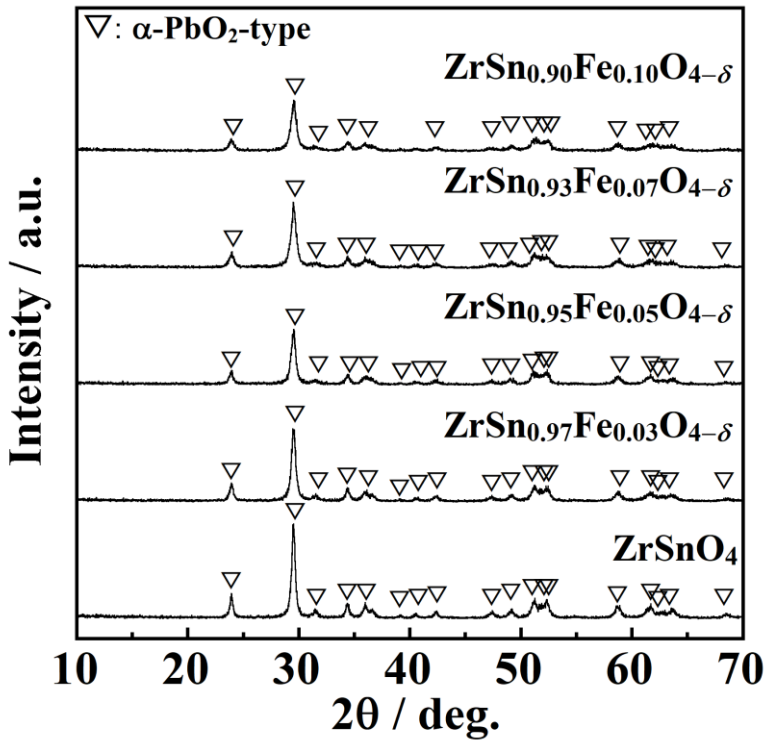

Figure 2-1. XRD patterns of the $ZrSn_{1-x}Fe_xO_{4-\delta}$ solids.

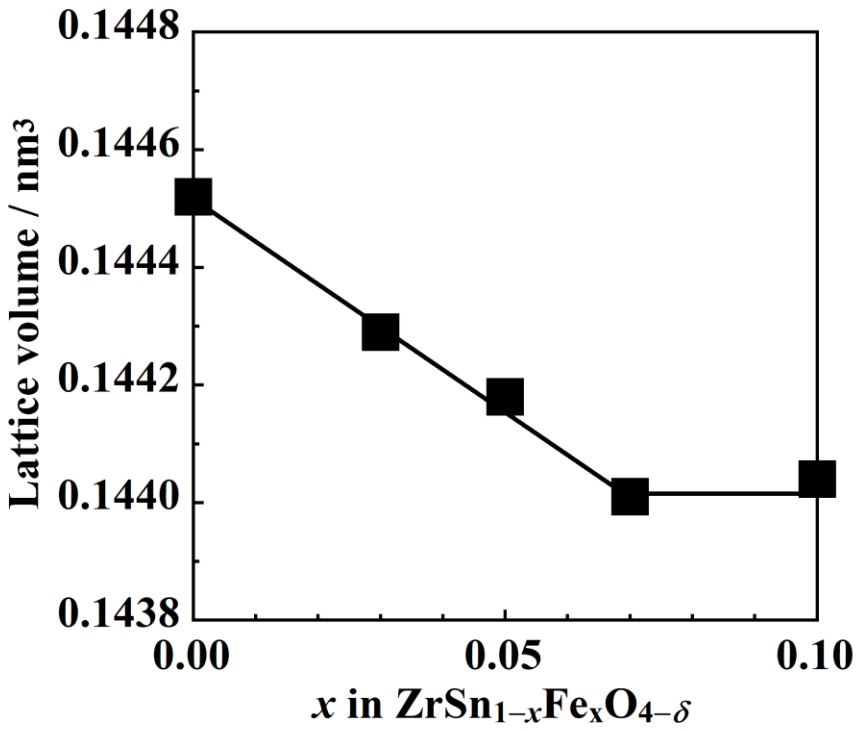

Figure 2-2. Compositional dependence of the lattice volume for $ZrSn_{1-x}Fe_xO_{4-\delta}$.

In order to investigate the effect of the $Fe^{2+/3+}$ introduction on the redox properties of $ZrSnO_4$, TPR measurement was performed for $ZrSn_{1-x}Fe_xO_{4-\delta}$, and the TPR profiles are shown in **Figure 2-3**. For $ZrSnO_4$, there were no obvious reduction peaks below 300 °C, whereas the shoulder peak was observed at the temperatures higher than 300 °C. In the cases of $ZrSn_{1-x}Fe_xO_{4-\delta}$, all the samples have one broad reduction peak (ca. 270 °C) below 300 °C, which were identified as the reduction of Fe^{3+} [38]. In the range of $x \leq 0.07$, the reduction peaks shifted toward lower temperatures with increasing the Fe content (x), and the lowest reduction temperature was obtained for the sample with $x = 0.07$ (259 °C). This acceleration of the oxygen release can be explained by the introduction of $Fe^{2+/3+}$ into $ZrSnO_4$, which improved the redox properties owing to the valence change of $Fe^{2+/3+}$ and generated oxygen vacancies for smooth oxide ion conduction. For $x = 0.10$, the reduction temperature shifted toward higher temperatures, due to amorphous phase of excess Fe component on the surface. Therefore, it is considered that the $x = 0.07$ sample exhibited the highest oxygen supply ability.

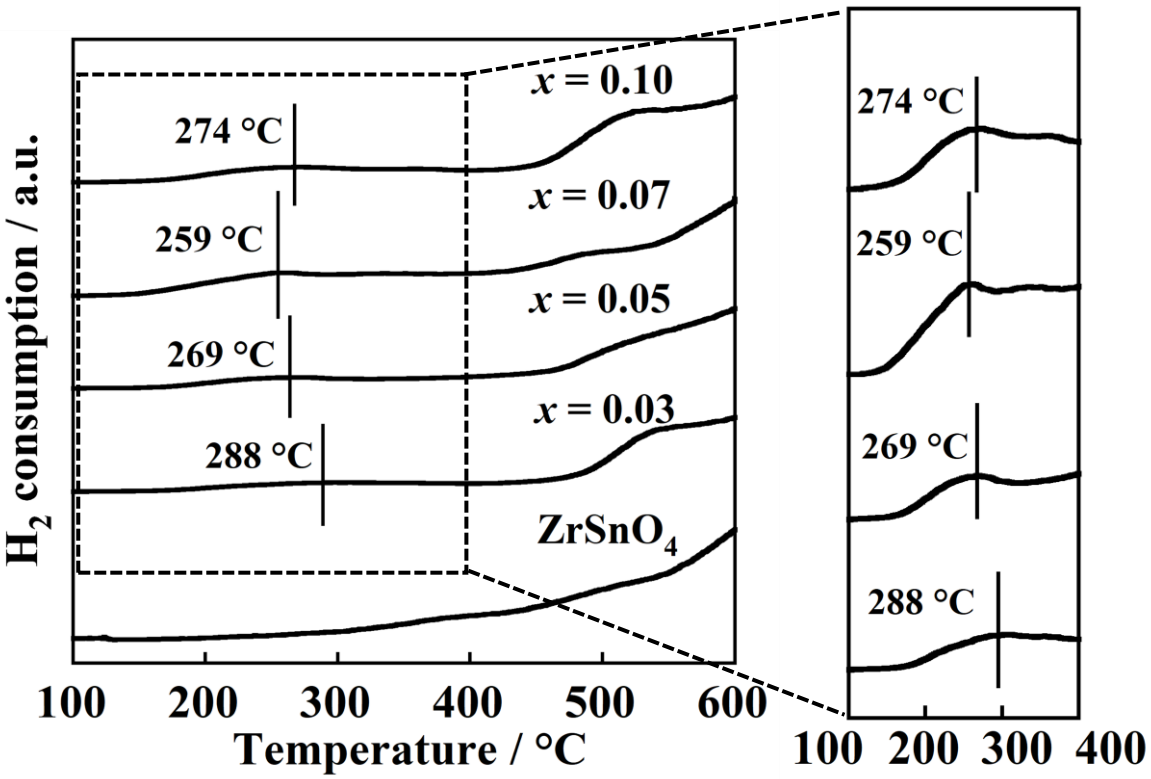

Figure 2-3. TPR profiles of $ZrSn_{1-x}Fe_xO_{4-\delta}$.

Figure 2-4 depicts the XRD patterns of $Co_3O_4/ZrSn_{1-x}Fe_xO_{4-\delta}$. For all the samples, the peaks were assigned to be the α-PbO_2-type phase and the spinel-type Co_3O_4 phase, suggesing that Co_3O_4 was supported onto $ZrSn_{1-x}Fe_xO_{4-\delta}$. **Table 2-1** shows the crystallite sizes of Co_3O_4 and $ZrSn_{1-x}Fe_xO_{4-\delta}$ estimated from the XRD results. For all the samples, the crystallite sizes of Co_3O_4 (ca. 7 nm) and $ZrSn_{1-x}Fe_xO_{4-\delta}$(ca. 26 nm) were almost the same, irrespective of the $Fe^{2+/3+}$ content (x).

Table 2-2 shows the measured compositions and the specific surface areas of the $Co_3O_4/ZrSn_{1-x}Fe_xO_{4-\delta}$ catalysts. The measured compositions were in good agreement with their feed values, within the experimental error. In addition, the specific surface areas of all the samples were similar (ca. 31 $m^2 \cdot g^{-1}$).

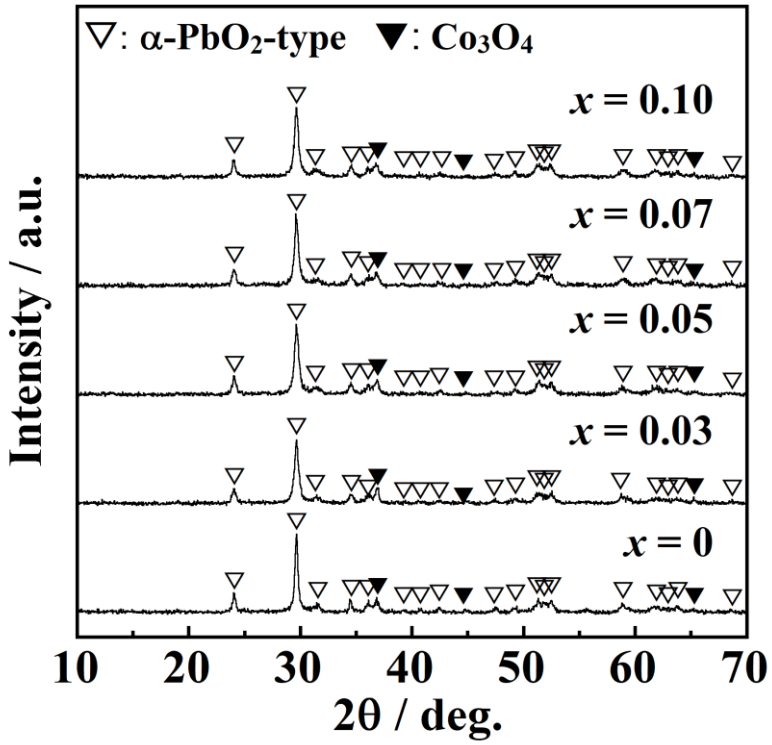

Figure 2-4. XRD patterns of the $Co_3O_4/ZrSn_{1-x}Fe_xO_{4-\delta}$ catalysts.

Table 2-1. Crystallite sizes of Co_3O_4 and $ZrSn_{1-x}Fe_xO_{4-\delta}$ for the $Co_3O_4/ZrSn_{1-x}Fe_xO_{4-\delta}$ catalysts

Catalyst	Co_3O_4 / nm	$ZrSn_{1-x}Fe_xO_{4-\delta}$ / nm
$x = 0$	7	30
$x = 0.03$	7	23
$x = 0.05$	6	24
$x = 0.07$	7	27
$x = 0.10$	8	24

Table 2-2. Measured composition and specific surface area of the $Co_3O_4/ZrSn_{1-x}Fe_xO_{4-\delta}$ catalysts

Feed composition	Measured composition	Specific surface area / $m^2 \cdot g^{-1}$
19wt% $Co_3O_4/ZrSnO_4$	19.3wt% $Co_3O_4/Zr_{1.05}Sn_{0.95}O_4$	31.6
19wt% $Co_3O_4/ZrSn_{0.97}Fe_{0.03}O_{4-\delta}$	19.7wt% $Co_3O_4/Zr_{1.04}Sn_{0.93}Fe_{0.03}O_{4-\delta}$	31.4
19wt% $Co_3O_4/ZrSn_{0.95}Fe_{0.05}O_{4-\delta}$	19.5wt% $Co_3O_4/Zr_{1.06}Sn_{0.89}Fe_{0.05}O_{4-\delta}$	30.4
19wt% $Co_3O_4/ZrSn_{0.93}Fe_{0.07}O_{4-\delta}$	19.2wt% $Co_3O_4/Zr_{1.07}Sn_{0.86}Fe_{0.07}O_{4-\delta}$	31.4
19wt% $Co_3O_4/ZrSn_{0.90}Fe_{0.10}O_{4-\delta}$	19.2wt% $Co_3O_4/Zr_{1.07}Sn_{0.84}Fe_{0.10}O_{4-\delta}$	32.5

Figure 2-5 presents the TPR profiles of the $Co_3O_4/ZrSn_{1-x}Fe_xO_{4-\delta}$ catalysts. The $Co_3O_4/ZrSnO_4$ catalyst exhibited two peaks at 293 °C and 349 °C, assigned as the reduction of surface Co^{3+} and bulk Co^{3+}, respectively [39]. These reduction peaks shifted toward lower temperatures with increasing the $Fe^{2+/3+}$ content for $x \leq 0.07$. This easier reduction of Co_3O_4 may be attributed to the improved oxygen supply ability of the $ZrSn_{1-x}Fe_xO_{4-\delta}$ solid. For the $x = 0.10$ catalyst, each reduction peak shifted toward higher temperatures compared to that for the $x = 0.07$ catalyst, which was related to the Fe based amorphous phase on the catalyst surface. From these results, the $x = 0.07$ catalyst showed the highest reducibility; that is, the oxygen release from Co_3O_4 was facilitated by the oxygen supply from the $ZrSn_{1-x}Fe_xO_{4-\delta}$ lattice.

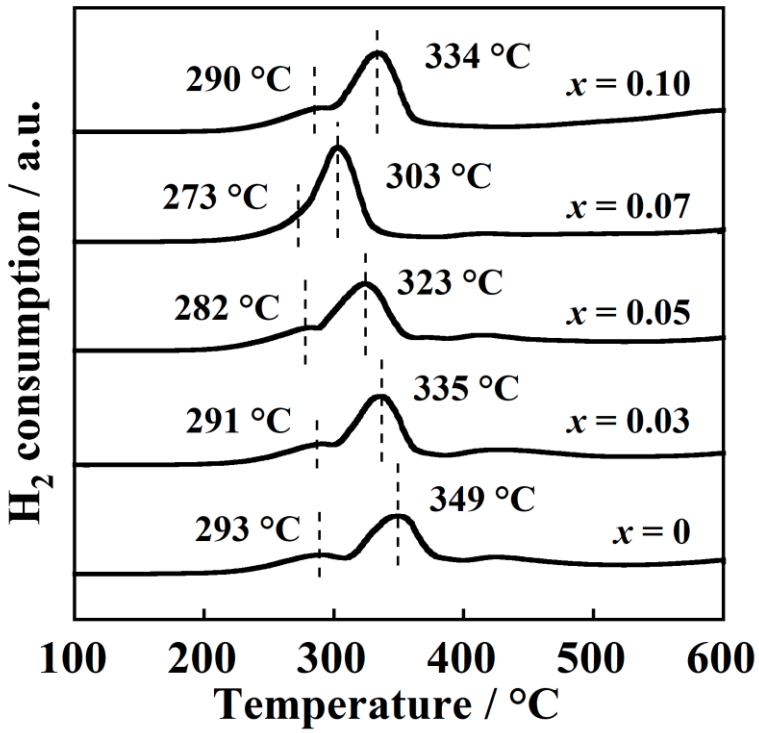

Figure 2-5. TPR profiles of the $Co_3O_4/ZrSn_{1-x}Fe_xO_{4-\delta}$ catalysts.

The temperature dependence of the N_2O conversion for $Co_3O_4/ZrSn_{1-x}Fe_xO_{4-\delta}$ are depicted in **Figure 2-6**. With the increase in x, the catalytic activity of the catalysts with $x \leq 0.07$ obviously enhanced, because the effective oxygen supply from inside the $ZrSn_{1-x}Fe_xO_{4-\delta}$ lattice toward Co_3O_4 facilitated the removal of adsorbed oxygen. On the other hand, the catalyst with $x = 0.10$ showed lower activity than that for $x = 0.07$, because of its decreased oxygen supply ability. Therefore, the $Co_3O_4/ZrSn_{0.93}Fe_{0.07}O_{4-\delta}$ catalyst exhibited the highest activity, where N_2O was completely decomposed at 500 °C. Although the $Rh/ZrSnO_4$ catalyst could decompose N_2O completely at 450 °C (as described in Chapter 1), it relies on the use of the noble metal Rh. The developed $Co_3O_4/ZrSn_{0.93}Fe_{0.07}O_{4-\delta}$ catalyst exhibited a high N_2O decomposition efficiency of 84% at the same temperature of 450 °C without using the noble metal.

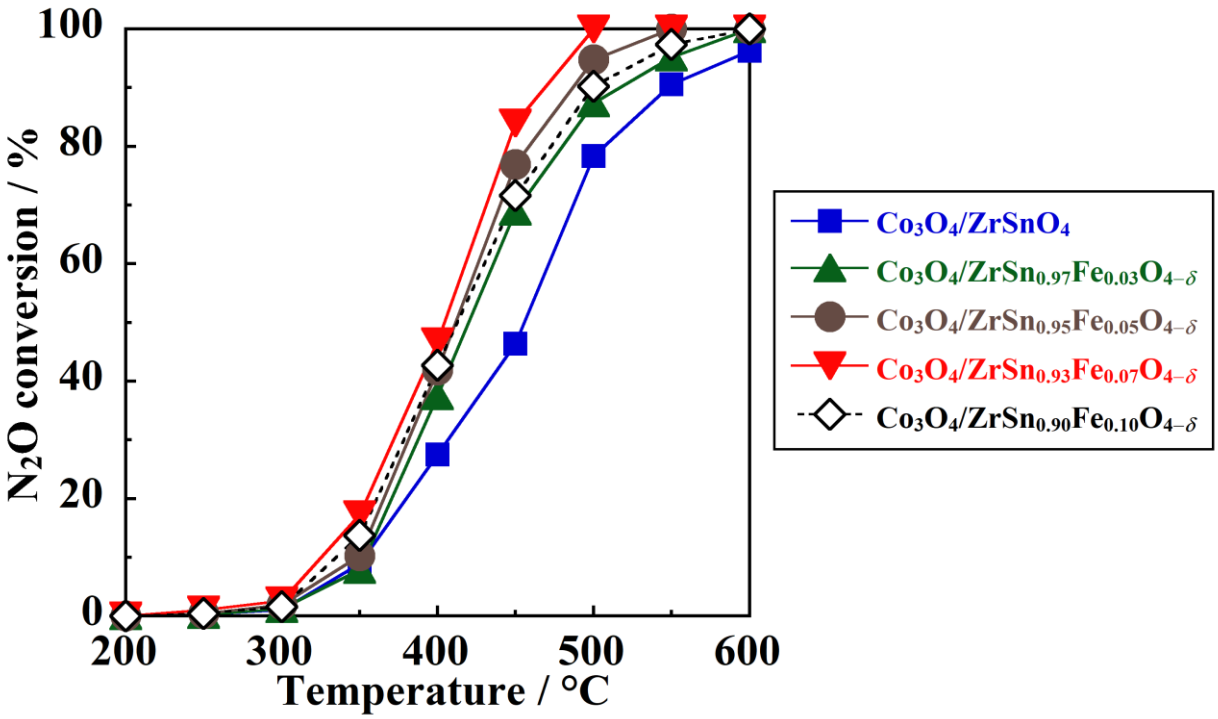

Figure 2-6. Temperature dependence of the N_2O conversion for the $Co_3O_4/ZrSn_{1-x}Fe_xO_{4-\delta}$ catalysts.

The effect of the Co_3O_4 loading amount on the catalytic activity was investigated. The XRD patterns of the *y* wt% $Co_3O_4/ZrSn_{0.93}Fe_{0.07}O_{4-\delta}$ (*y* = 11, 18, 19, 20, 27) catalysts are shown in **Figure2-7**. For each sample, peaks identified as the α-PbO_2-type structure and the Co_3O_4 phase were observed without any peaks caused by impurities.

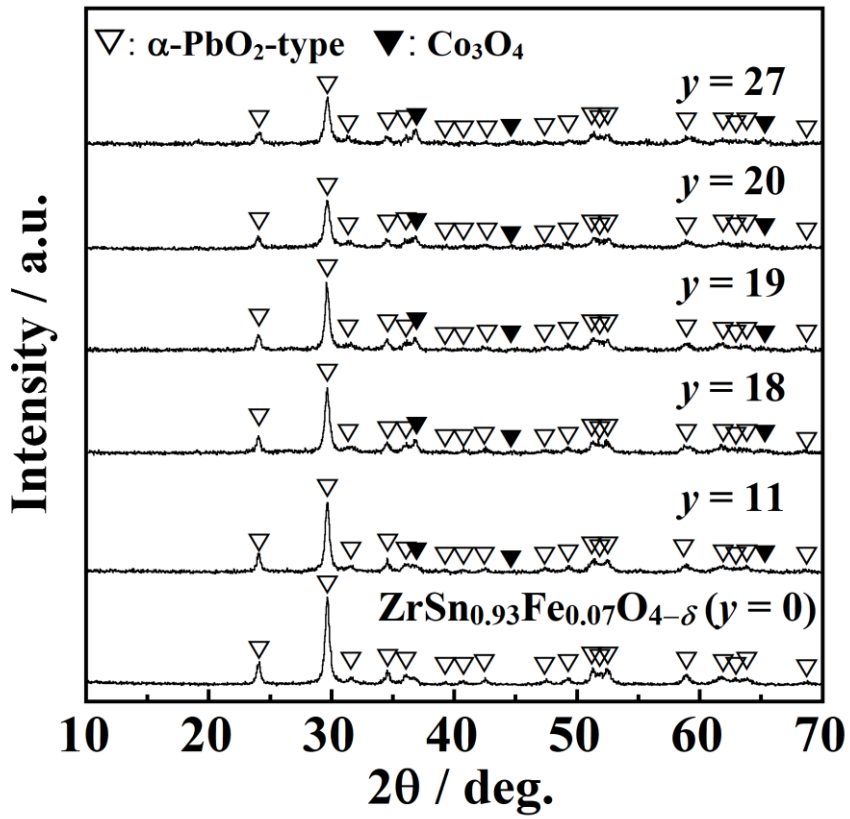

Figure 2-7. XRD patterns of the *y* wt% $Co_3O_4/ZrSn_{0.93}Fe_{0.07}O_{4-\delta}$ catalysts.

Figure 2-8 shows the temperature dependence of the N_2O conversion for the y wt% $Co_3O_4/ZrSn_{0.93}Fe_{0.07}O_{4-\delta}$ catalysts. With increasing the Co_3O_4 loading amount (y), the catalytic activity improved up to y = 19. This phenomenon can be explained by the increase in the amount of the Co_3O_4 activator. For the catalysts with y > 19, the catalytic activity decreased probably due to the aggregation of Co_3O_4. Therefore, the loading amount of the Co_3O_4 activator was optimized to be 19 wt%.

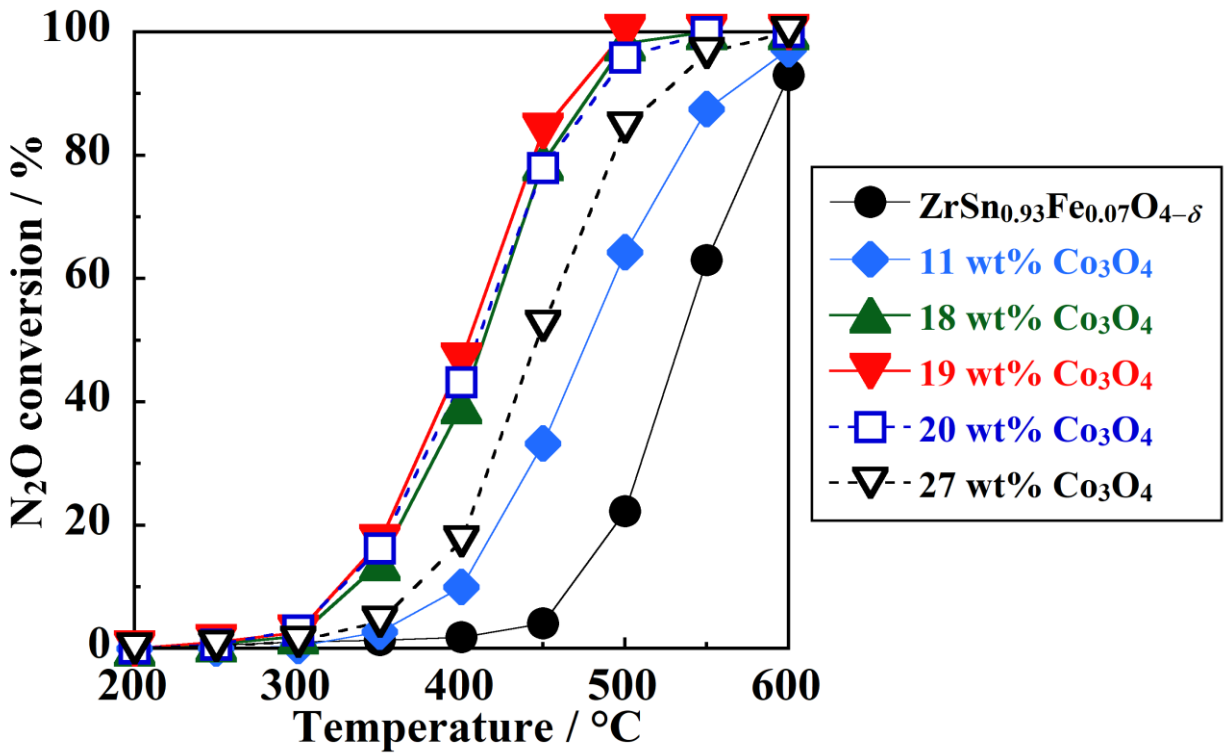

Figure 2-8. Temperature dependence of the N_2O conversion for the y wt% $Co_3O_4/ZrSn_{0.93}Fe_{0.07}O_{4-\delta}$ catalysts.

2.4. Conclusion

In this chapter, in order to develop noble-metal-free catalysts with high catalytic activity for N_2O direct decomposition, the $Co_3O_4/ZrSn_{1-x}Fe_xO_{4-\delta}$ catalysts were prepared. The introduction of $Fe^{2+/3+}$ ions into the $ZrSnO_4$ lattice enhanced the N_2O decomposition activity, because of the redox properties of the $Fe^{2+/3+}$ couple and the generation of oxygen vacancies for the smooth oxide ion conduction. Among the prepared catalysts, the 19 wt% $Co_3O_4/ZrSn_{0.93}Fe_{0.07}O_{4-\delta}$ catalyst exhibited the highest activity and achieved complete decomposition of N_2O at 500 °C without using noble metals.

Chapter 3

$ZrSnO_4$ Based Catalysts with Durability against Oxygen Gas and Water Vapor

3.1. Introduction

In Chapter 2, 19 wt% $Co_3O_4/ZrSn_{0.93}Fe_{0.07}O_{4-\delta}$ completely decomposed N_2O at 500 °C, while it does not contain noble metals. However, the spinel-type Co_3O_4 catalyst is reported to have low durability against coexisting gases of oxygen gas and water vapor [40]. Here, practically applied catalysts are often exposed to coexisting gases; e.g. 4 vol% O_2 and 2–3 vol% H_2O vapor during adipic acid and nitric acid production [41]. Therefore, the development of catalysts with high durability against coexisting gases of oxygen gas and water vapor is desired.

This chapter aims the development of novel catalysts with high durability against coexisting gases of O_2 and H_2O vapor. To this end, the doping of $Co^{2+/3+}$ was carried out into the $ZrSnO_4$ lattice, instead of the loading of $Co^{2+/3+}$ as Co_3O_4 with low durability. The doping of $Co^{2+/3+}$ was expected to improve the redox properties due to two types of valence states of Co^{2+} and Co^{3+} and to increase oxygen vacancies through the replacement of the Sn^{4+} site for low-valent $Co^{2+/3+}$. In addition, since the ionic-size of Sn^{4+} was closer to Co^{2+} than to Fe^{2+} (Sn^{4+}: 0.083 nm, Co^{2+}: 0.079 nm, Fe^{2+}: 0.075 nm, CN = 6) [37], the high amount of dopant is expected to be introduced into the Sn^{4+} site in the $ZrSnO_4$ lattice, compared to the case of the $Fe^{2+/3+}$ doped $ZrSnO_4$ series. Therefore, $ZrSn_{1-x}Co_xO_{4-\delta}$ catalysts were prepared, and their N_2O direct decomposition activities and durability against coexisting gases of O_2 and H_2O vapor were investigated.

3.2. Experimental Procedure

The $ZrSn_{1-x}Co_xO_{4-\delta}$ powders were prepared by a co-precipitation method by using starting materials of zirconium (IV) oxynitrate dihydrate ($ZrO(NO_3)_2 \cdot 2H_2O$, Kishida Chemical, ≥ 99.0%) powder, tin (II) oxalate (SnC_2O_4, Sigma-Aldrich, 99%) powder, and cobalt (II) nitrate hexahydrate ($Co(NO_3)_2 \cdot 6H_2O$, Kishida Chemical, ≥ 98.0%) powder, where a feed Zr:Sn:Co molar ratio was $1.3:(1-x):x$. The subsequent experimental methods are the same as described in Chapter 1.

The obtained sample compositions were determined by using XRF (Supermini200, Rigaku). The BET specific surface area was determined by using a Micromeritics TriStar 3000 analyzer (Shimadzu). The crystal structures were identified through XRD (SmartLab, Rigaku) with Cu Kα radiation. The lattice volumes were calculated through refining the XRD peak angles using α-alumina as the internal standard. TPR measurements were conducted under a reducing gas flow (5 vol% H_2 - 95 vol% Ar at 50 $mL \cdot min^{-1}$) at a heating rate of 5 $°C \cdot min^{-1}$ over 0.035 g of catalysts (BELCAT-B, MicrotracBEL). The oxidation sates of Co species were analyzed by XPS (PHI5000 VersaProbe II, ULVAC-PHI) analysis with Al Kα radiation, where the effect of charging on the binding energies was refined by the C 1s peak (284.6 eV). The XPS spectrum was fitted using a Shirley background and Gaussian–Lorentzian line shapes.

The catalytic activity for N_2O direct decomposition was carried out according to Chapter 1. The effect of the coexistence of O_2 and H_2O vapor on the activity was investigated by mixing O_2 gas with the reactant gas (0.5 vol% N_2O - 99.5 vol% He) and bubbling the gas into deionized water. During the durability test, the total flow rate of the mixed gas was set at 60 $mL \cdot min^{-1}$.

3.3. Results and Discussion

The measured compositions of the $ZrSn_{1-x}Co_xO_{4-\delta}$ catalysts are listed in **Table 3-1**. For all the samples, the Co content in the measured composition was lower than that in the feed composition, probably due to the generation of a water-soluble complex (e.g., $Co(NH_3)_6^{3+}$) during the co-precipitation process. Nevertheless, an almost linear relationship was obtained between the Co content in the measured values and that in the feed values. Hereafter, the Co contents (x) were expressed using measured values; that is, $Zr_{1.07}Sn_{0.93}O_4$, $Zr_{1.09}Sn_{0.87}Co_{0.04}O_{4-\delta}$, $Zr_{1.15}Sn_{0.78}Co_{0.07}O_{4-\delta}$, $Zr_{1.17}Sn_{0.73}Co_{0.10}O_{4-\delta}$, and $Zr_{1.24}Sn_{0.63}Co_{0.13}O_{4-\delta}$, were denoted as $ZrSn_{1-x}Co_xO_{4-\delta}$ (x = 0, 0.04, 0.07, 0.10, and 0.13), respectively, in Chapter 3. The BET specific surface areas of the $ZrSn_{1-x}Co_xO_{4-\delta}$ catalysts are also listed in **Table 3-1**. All the samples showed similar specific surface areas of ca. 30 $m^2 \cdot g^{-1}$.

Table 3-1. Measured composition and specific surface area of the $ZrSn_{1-x}Co_xO_{4-\delta}$ catalysts

Feed composition	Measured composition	Specific surface area / $m^2 \cdot g^{-1}$
$ZrSnO_4$	$Zr_{1.07}Sn_{0.93}O_4$	30.2
$ZrSn_{0.90}Co_{0.10}O_{4-\delta}$	$Zr_{1.09}Sn_{0.87}Co_{0.04}O_{4-\delta}$	29.6
$ZrSn_{0.80}Co_{0.20}O_{4-\delta}$	$Zr_{1.15}Sn_{0.78}Co_{0.07}O_{4-\delta}$	27.2
$ZrSn_{0.70}Co_{0.30}O_{4-\delta}$	$Zr_{1.17}Sn_{0.73}Co_{0.10}O_{4-\delta}$	32.2
$ZrSn_{0.60}Co_{0.40}O_{4-\delta}$	$Zr_{1.24}Sn_{0.63}Co_{0.13}O_{4-\delta}$	29.7

The XRD patterns of the $ZrSn_{1-x}Co_xO_{4-\delta}$ (x = 0.04, 0.07, 0.10, 0.13) catalysts are shown in **Figure 3-1**. The catalysts with $x \leq 0.10$ exhibited a single-phase α-PbO_2-type structure. For the catalyst with x = 0.13, no peak corresponding to the α-PbO_2-type phase was observed, and only the cubic ZrO_2 phase was detected. **Figure 3-2** displays the compositional dependence of the lattice volume for the catalysts with $x \leq 0.10$. With increasing x, the lattice volume of the α-PbO_2-type phase decreased monotonously with increasing the $Co^{2+/3+}$ content (x) up to x = 0.10, indicating that the Sn^{4+} site (0.083 nm, CN = 6) [37] was successfully replaced for the smaller $Co^{2+/3+}$ ions (Co^{2+}: 0.079 nm, Co^{3+}: 0.069 nm, CN = 6) [37]. Here, as shown in **Table 3-1**, the content of Zr^{4+} having large ionic-size (0.086 nm, CN = 6) [37] was also increased with increasing the $Co^{2+/3+}$ content, which supports that the lattice shrinkage was mainly affected by the introduction of the small ionic-size of $Co^{2+/3+}$.

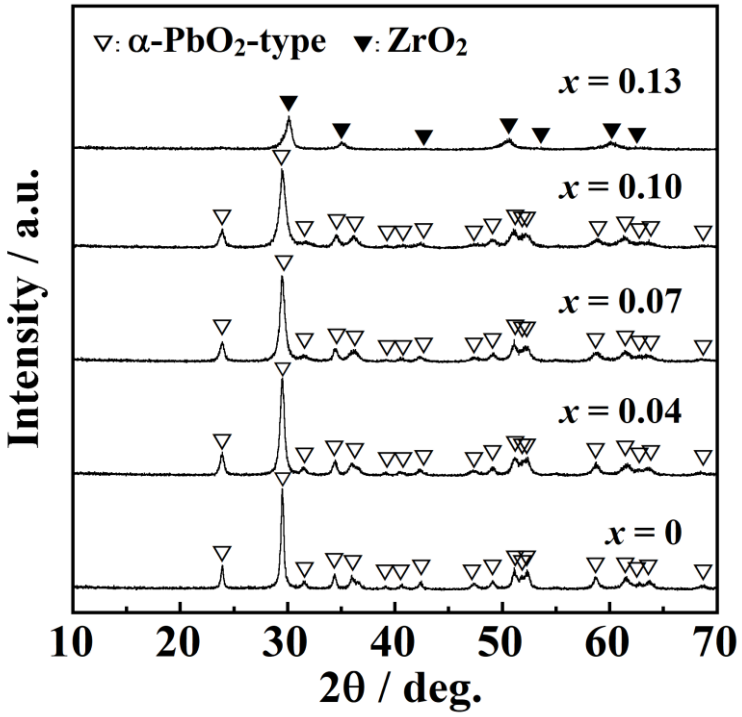

Figure 3-1. XRD patterns of the $ZrSn_{1-x}Co_xO_{4-\delta}$ catalysts.

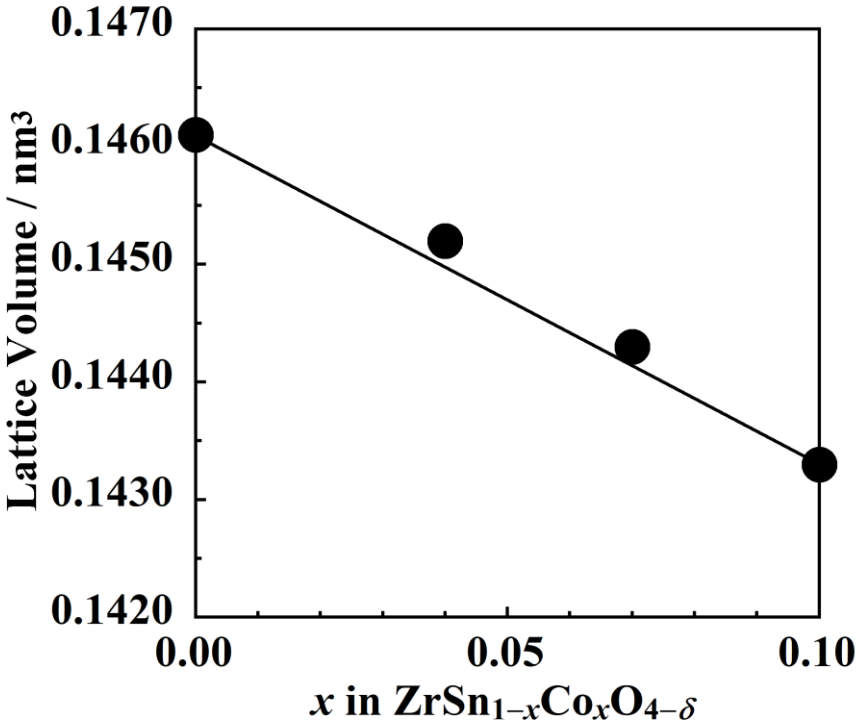

Figure 3-2. Compositional dependence of the lattice volume for $ZrSn_{1-x}Co_xO_{4-\delta}$.

Figure 3-3 presents the XPS spectra of Co 2p core levels for $ZrSn_{1-x}Co_xO_{4-\delta}$ (x = 0.04, 0.07, 0.10), where the fitting parameters are listed in **Table 3-2**. Since the Co $2p_{1/2}$ and Co $2p_{3/2}$ peaks could be divided into Co^{2+} and Co^{3+} peaks, the ratios of $Co^{2+}/(Co^{2+}+Co^{3+})$ were estimtated (**Table 3-3**). The $Co^{2+}/(Co^{2+}+Co^{3+})$ ratio was increased with increasing x, indicating that more oxygen vacancies were generated. The charge transfer between Co^{2+} and Co^{3+} can accelerate the redox properties.

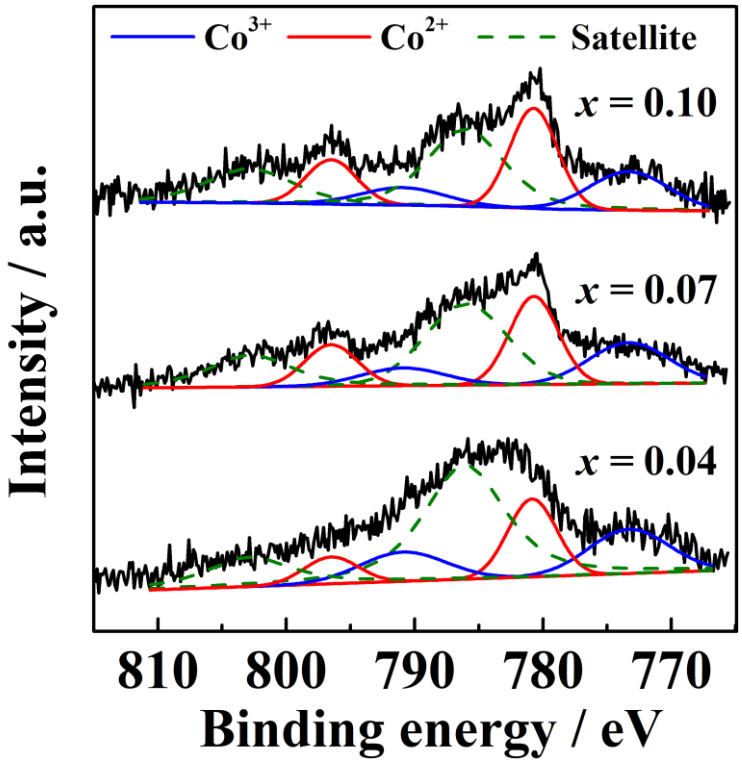

Figure 3-3. XPS spectra of Co 2p core levels for $ZrSn_{1-x}Co_xO_{4-\delta}$.

Table 3-2. Fitting parameters of the Co 2p XPS spectra for the $ZrSn_{1-x}Co_xO_{4-\delta}$ catalysts

Catalyst	χ^2	Peak	Position / eV	FWHM / eV	Area / %
$Zr_{1.09}Sn_{0.87}Co_{0.04}O_{4-\delta}$	0.128	Co^{3+} $2p_{3/2}$	773.3	7.3	13.2
(x = 0.04)		Co^{2+} $2p_{3/2}$	780.8	4.4	14.1
		Satellite	786.1	7.5	44.9
		Co^{3+} $2p_{1/2}$	790.9	7.8	9.3
		Co^{2+} $2p_{1/2}$	796.5	4.9	5.3
		Satellite	802.9	7.8	13.1
$Zr_{1.13}Sn_{0.80}Co_{0.07}O_{4-\delta}$	0.061	Co^{3+} $2p_{3/2}$	773.3	7.3	15.2
(x = 0.07)		Co^{2+} $2p_{3/2}$	780.7	4.5	19.8
		Satellite	786.0	7.6	32.4
		Co^{3+} $2p_{1/2}$	790.9	7.8	6.9
		Co^{2+} $2p_{1/2}$	796.5	4.8	10.1
		Satellite	802.8	7.7	15.6
$Zr_{1.17}Sn_{0.73}Co_{0.10}O_{4-\delta}$	0.019	Co^{3+} $2p_{3/2}$	773.3	7.2	13.7
(x = 0.10)		Co^{2+} $2p_{3/2}$	780.7	4.4	21.6
		Satellite	786.0	7.0	31.7
		Co^{3+} $2p_{1/2}$	790.9	7.8	6.7
		Co^{2+} $2p_{1/2}$	796.5	4.7	10.3
		Satellite	802.8	7.9	16.0

Table 3-3. Ratio of $Co^{2+}/(Co^{2+}+Co^{3+})$ for $ZrSn_{1-x}Co_xO_{4-\delta}$

Catalyst	$Co^{2+}/(Co^{2+}+Co^{3+})$
x = 0.04	51.6 %
x = 0.07	56.6 %
x = 0.10	61.2 %

Figure 3-4 shows the TPR profiles of $ZrSn_{1-x}Co_xO_{4-\delta}$ ($x \leq 0.10$). For $ZrSnO_4$, there were no obvious reduction peaks below 300 °C, whereas the shoulder peak was observed at the temperatures higher than 300 °C. The $Co^{2+/3+}$ doped samples had two reduction peaks below 300 °C, identified as the reduction of surface Co^{3+} and bulk Co^{3+} [42]. While no remarkable change was observed for the bulk reduction peak (ca. 275 °C) because of its low intensity and broad shape, the surface reduction peak (ca. 210 °C) decreased obviously with increasing *x*. These behaviors were attributed to the improved redox properties. The highest oxygen supply ability was obtained for $Zr_{1.17}Sn_{0.73}Co_{0.10}O_{4-\delta}$.

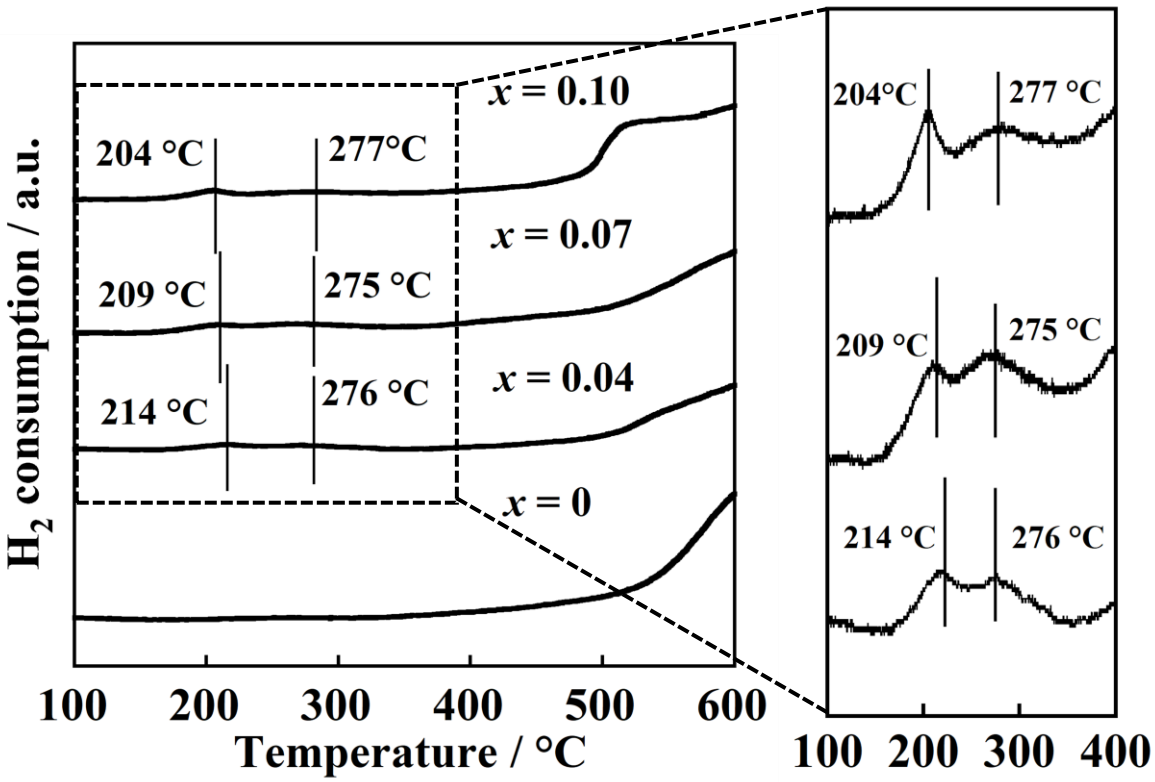

Figure 3-4. TPR profiles of the $ZrSn_{1-x}Co_xO_{4-\delta}$ catalysts.

Figure 3-5 shows the temperature dependence of the N_2O conversion for $ZrSn_{1-x}Co_xO_{4-\delta}$ with the data of $ZrSn_{0.93}Fe_{0.07}O_{4-\delta}$. With increasing the Co content (x), the catalytic activity increased, and the highest activity was obtained for the x = 0.10 catalyst, in which N_2O was completely decomposed at 550 °C. This enhanced activity was attributed to the high oxygen supply ability that facilitated the removal of adsorbed oxygen, which is known to be the rate-determining step, as described in the General Introduction section. In addition, oxygen vacancies formed by replacing the Sn^{4+} site for lower-valent $Co^{2+/3+}$ could act as catalytically active sites. In contrast, the x = 0.13 catalyst with the cubic ZrO_2 phase showed low activity compared to that of the x = 0.10 catalyst with the α-PbO_2-type phase. Moreover, the $Co^{2+/3+}$ doped catalyst of $Zr_{1.17}Sn_{0.73}Co_{0.10}O_{4-\delta}$ exhibited higher catalytic activity than that of the $Fe^{2+/3+}$ doped catalyst ($ZrSn_{0.93}Fe_{0.07}O_{4-\delta}$).

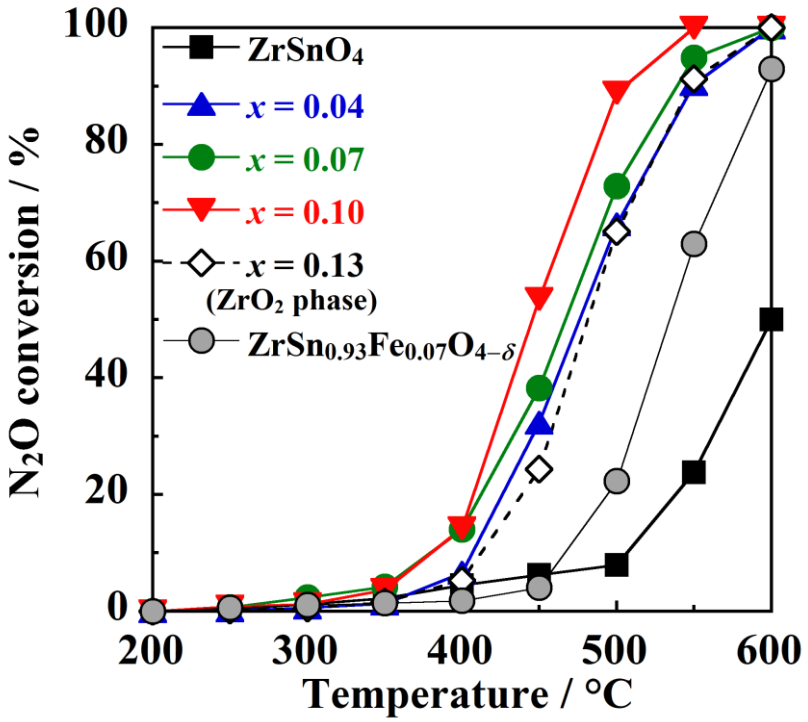

Figure 3-5. Temperature dependence of N_2O conversion for $ZrSn_{1-x}Co_xO_{4-\delta}$ and $ZrSn_{0.93}Fe_{0.07}O_{4-\delta}$.

The durability test against the coexisting gases of oxygen gas and water vapor was investigated. **Figure 3-6** shows the N_2O conversion in the presence of 10 vol% oxygen gas and 3 vol% water vapor at 500 °C as a function of time for the x = 0.10 catalyst ($Zr_{1.17}Sn_{0.73}Co_{0.10}O_{4-\delta}$), with the data of $Co_3O_4/ZrSn_{0.93}Fe_{0.07}O_{4-\delta}$. Although $Co_3O_4/ZrSn_{0.93}Fe_{0.07}O_{4-\delta}$ completely decomposed N_2O before the durability test, it was drastically deactivated by the exposure of O_2 and H_2O vapor. After 6 h, the N_2O conversion for $Co_3O_4/ZrSn_{0.93}Fe_{0.07}O_{4-\delta}$ decreased down to 47%; that is, the decrease in the N_2O conversion on going from 0 to 6 h was 53% (100% → 47%). For $Zr_{1.17}Sn_{0.73}Co_{0.10}O_{4-\delta}$, while the N_2O conversion before the test (87%) was lower than that of $Co_3O_4/ZrSn_{0.93}Fe_{0.07}O_{4-\delta}$ (100%), the high catalytic activity maintained even in the presence of O_2 and H_2O vapor, where the slight decrease might be affected by the competition of coexisting gases with N_2O for adsorption on the catalytic active sites. The decrease in the N_2O conversion on going from 0 to 6 h was 14% (87% → 73%), which is appreciably lower than that for $Co_3O_4/ZrSn_{0.93}Fe_{0.07}O_{4-\delta}$ (53%). Thus, the $Co^{2+/3+}$ doping was effective to obtain the catalyst with high durability, compared to the $Co^{2+/3+}$ loading as Co_3O_4 with low durability. It is reported that Co_3O_4 was deactivated by the adsorption of O_2 and/or H_2O molecules on the surface $Co^{2+/3+}$ ions [43]. In the case of $Zr_{1.17}Sn_{0.73}Co_{0.10}O_{4-\delta}$, since the $Co^{2+/3+}$ ions were introduced into the crystal lattice, the deactivation related to the surface Co species could be suppressed. Furthermore, the N_2O conversion after 6 h for $Zr_{1.17}Sn_{0.73}Co_{0.10}O_{4-\delta}$ (73%) was considerably higher than that for $Co_3O_4/ZrSn_{0.93}Fe_{0.07}O_{4-\delta}$ (47%).

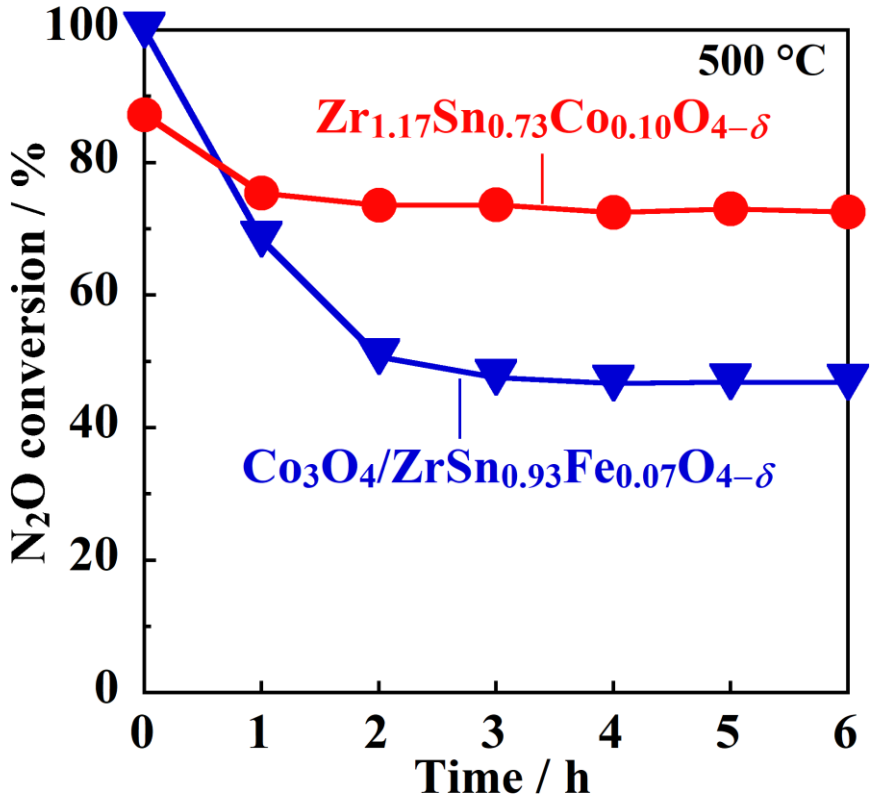

Figure 3-6. N_2O conversion in the presence of 10 vol% oxygen gas and 3 vol% water vapor as a function of time for $Zr_{1.17}Sn_{0.73}Co_{0.10}O_{4-\delta}$ and $Co_3O_4/ZrSn_{0.93}Fe_{0.07}O_{4-\delta}$.

3.4. Conclusion

In this chapter, in order to develop novel catalysts with high durability against coexisting gases of O_2 and H_2O vapor, the doping of $Co^{2+/3+}$ into the $ZrSnO_4$ lattice was conducted, instead of the loading of $Co^{2+/3+}$ as Co_3O_4 with low durability; i.e., $ZrSn_{1-x}Co_xO_{4-\delta}$ catalysts were prepared. The introduction of $Co^{2+/3+}$ into the $ZrSnO_4$ lattice resulted in the enhanced catalytic activity for direct decomposition of N_2O. The $Zr_{1.17}Sn_{0.73}Co_{0.10}O_{4-\delta}$ catalyst exhibited the highest activity and achieved complete decomposition of N_2O at 550 °C. Furthermore, the catalyst of $Zr_{1.17}Sn_{0.73}Co_{0.10}O_{4-\delta}$ showed high durability against coexisting gases of 10 vol% oxygen and 3 vol% water vapor. The decrease in the N_2O conversion at 500 °C on going from 0 to 6 h was 14%, which was appreciably lower than that for $Co_3O_4/ZrSn_{0.93}Fe_{0.07}O_{4-\delta}$ (53%).

Summary

In this doctoral thesis, novel catalysts based on zirconium-tin oxide were developed for effective direct decomposition of nitrous oxide. The results obtained through this study are summarized as follows:

Chapter 1

In order to develop novel catalysts with high activity, $ZrSnO_4$ was focused as a promoter to facilitate N_2O decomposition over the Rh activator. Among the *x* wt% Rh/$ZrSnO_4$ catalysts, the 1.0 wt% Rh/$ZrSnO_4$ catalyst exhibited the highest activity and was able to completely decompose N_2O at 450 °C. Furthermore, $ZrSnO_4$ showed the higher oxygen supply ability than those of SnO_2, ZrO_2, and Al_2O_3, likely because of the redox properties through the valence change of $Sn^{4+/2+}$ and the oxygen vacancies for oxide ion migration formed by the coexistence of Sn^{2+}. The high oxygen supply ability of $ZrSnO_4$ contributed to the high catalytic activity for 1.0 wt% Rh/$ZrSnO_4$ compared to those of 1.0 wt% Rh/SnO_2, 1.0 wt% Rh/ZrO_2, and 1.0 wt% Rh/Al_2O_3.

Chapter 2

For the development of noble-metal-free catalysts, spinel-type Co_3O_4 was selected as an activator instead of Rh. Furthermore, $Fe^{2+/3+}$ ions were introduced into the $ZrSnO_4$ lattice to facilitate N_2O decomposition over the Co_3O_4 activator. The $Fe^{2+/3+}$ introduction improved the oxygen supply

ability, likely due to the redox cycle ($Fe^{2+/3+}$) and the smooth oxide ion conduction via the oxygen vacancies generated by the replacement of the Sn^{4+} site for lower-valent $Fe^{2+/3+}$. Among the prepared catalysts, 19 wt% $Co_3O_4/ZrSn_{0.93}Fe_{0.07}O_{4-\delta}$ exhibited the highest activity and achieved complete decomposition of N_2O at 500 °C without noble metal.

Chapter 3

In order to develop novel catalysts with high durability against coexisting gases of O_2 and H_2O vapor, the $Co^{2+/3+}$ doping was carried out into the $ZrSnO_4$ lattice, instead of the $Co^{2+/3+}$ loading as Co_3O_4 with low durability. The $Co^{2+/3+}$ doping enhanced the oxygen supply ability, due to the improved redox properties caused by $Co^{2+/3+}$ and the increased amount of oxygen vacancies owing to lower-valent $Co^{2+/3+}$ compared to Sn^{4+}, which contributed to the high catalytic activity. Among the prepared catalysts, the $Zr_{1.17}Sn_{0.73}Co_{0.10}O_{4-\delta}$ catalyst exhibited the highest activity and achieved complete decomposition of N_2O at 550 °C. Moreover, the $Zr_{1.17}Sn_{0.73}Co_{0.10}O_{4-\delta}$ catalyst showed high durability against coexisting gases of 10 vol% oxygen gas and 3 vol% water vapor; that is, the decrease in the N_2O conversion at 500 °C on going from 0 to 6 h was 14%, lower than that for $Co_3O_4/ZrSn_{0.93}Fe_{0.07}O_{4-\delta}$ (53%).

References

[1] R. E. Dickinson and R. J. Cicerone, *Nature*, **319**, 109 (1986).

[2] C. Tricot and A. Berger, *Clim. Dyn.*, **2**, 39 (1987).

[3] A. R. Ravishankara, J. S. Daniel, and R. J. Cicerone, *Science*, **326**, 123 (2009).

[4] J. Pérez-Ramírez, *Appl. Catal. B: Environ.*, **70**, 31 (2007).

[5] H. Tian, R. Xu, J. G. Canadell, R. L. Thompson, W. Winiwarter, P. Suntharalingam, E. A. Davidson, P. Ciais, R. B. Jackson, G. Janssens-Maenhout, et al., *Nature*, **586**, 248 (2020).

[6] M. Takagi, T. Kawai, M. Soma, T. Onishi, and K. Tamaru, *J. Catal.*, **50**, 441 (1977).

[7] G. Busca, L. Lietti, G. Ramis, and F. Berti, *Appl. Catal. B: Environ.*, **18**, 1 (1998).

[8] X. Zhang, Q. Shen, C. He, C. Ma, J. Cheng, L. Li, and Z. Hao, *ACS Catal.*, **2**, 512 (2012).

[9] M. Galle, D. W. Agar, and O. Watzenberger, *Chem. Eng. Sci.*, **56**, 1587 (2001).

[10] K. Yuzaki, T. Yarimizu, K. Aoyagi, S. I. Ito, and K. Kunimori, *Catal. Today*, **45**, 129 (1998).

[11] P. H. Ho, M. Jabłońska, R. Palkovits, E. Rodríguez-Castellón, F. Ospitali, G. Fornasari, G. Vaccari, and P. Benito, *Chem. Eng. J.*, **379**, 122259 (2020).

[12] Y. Jing, C. He, N. Zhang, Y. Murano, R. Toyoshima, H. Kondoh, Y. Kageyama, H. Inomata, T. Toyao, and K. I. Shimizu, *ACS Catal.*, **13**, 12983 (2023).

[13] M. Hussain, D. Fino, and N. Russo, *J. Hazard. Mater.*, **211**, 255 (2012).

[14] G. Centi, A. Galli, B. E. A. Montanari, S. Perathoner, and A. Vaccaria, *Catal. Today*, **35**, 113 (1997).

[15] N. Nunotani, R. Nagai, and N. Imanaka, *Catal. Commun.*, **87**, 53 (2016).

[16] C. Huang, Z. Ma, C. Miao, Y. Yue, W. Hua, and Z. Gao, *RSC Adv.*, **7**, 4243 (2017).

[17] Y. Jing, K. Taketoshi, N. Zhang, C. He, T. Toyao, Z. Maeno, T. Ohori, N. Ishikawa, and K. I. Shimizu, *ACS Catal.*, **12**, 6325 (2022).

[18] L. Xue, C. Zhang, H. He, and Y. Teraoka, *Appl. Catal. B: Environ.,* **75**, 167 (2007).

[19] Y. Xiong, Y. Zhao, X. Qi, J. Qi, Y. Cui, H. Yu, and Y. Cao, *Environ. Sci. Technol.*, **55**, 13335 (2021).

[20]J. Sun, X. Wang, J. Cao, Y. Shu, Y. Liu, Q. Fu, and C. Pan, *ACS Appl. Energy Mater.*, **4**, 8496 (2021).

[21] F. Zhao, D. Wang, X. Li, Y. Yin, C. Wang, L. Qiu, J. Yu, and H. Chang, *Ind. Eng. Chem. Res.*, **61**, 13854 (2022).

[22] N. Russo, D. Mescia, D. Fino, G. Saracco, and V. Specchia, *Ind. Eng. Chem. Res.*, **46**, 4226 (2007).

[23] S. Kumar, A. Vinu, J. Subrt, S. Bakardjieva, S. Rayalu, Y. Teraoka, and N. Labhsetwar, *Catal. Today*, **198**, 125 (2012).

[24] C. Huang, Y. Zhu, X. Wang, X. Liu, J. Wang, and T. Zhang, *J. Catal.*, **347**, 9 (2017).

[25] N. Richards, J. H. Carter, L. A. Parker, S. Pattisson, D. G. Hewes, D. J. Morgan, T. E. Davies, N. F. Dummer, S. Folunski, and G. J. Hutchings, *ACS Catal.*, **10**, 5430 (2020).

[26] M. Tian, A. Wang, X. Wang, Y. Zhu, and T. Zhang, *Appl. Catal. B: Environ.*, **92**, 437 (2009).

[27] Y. Zhang, X. Wang, Y. Zhu, and T. Zhang, *Appl. Catal. B: Environ.*, **129**, 382 (2013).

[28] M. Santiago and J. Pérez-Ramírez, *Environ. Sci. Technol.*, **41**, 1704 (2007).

[29] M. Santiago, J. C. Groen, and J. Pérez-Ramírez, *J. Catal.*, **257**, 152 (2008).

[30] A. Ghahri, F. Golbabaei, L. Vafajoo, S. M. Mireskandari, M. Yaseri, and S. J. Shahtaheri, *Int. J. Environ. Res.*, **11**, 327 (2017).

[31] T. Zhang, Y. Qiu, G. Liu, J. Chen, Y. Peng, B. Liu, and J. Li, *J. Catal.*, **392**, 322 (2020).

[32] B. Kang, M. Li, Z. Di, X. Guo, Y. Wei, J. Jia, and R. Zhang, *Catal. Today*, **402**, 17 (2022).

[33] K. M. Farhan, A. N. Thabassum, T. M. Ismail, and P. K. Sajith, *Catal. Sci. Technol.*, **12**, 1466 (2022).

[34] F. Kapteijn, J. Rodriguez-Mirasol, and J. A. Moulijn, *Appl. Catal. B: Environ.*, **9**, 25 (1996).

[35] M. Konsolakis, *ACS Catal.*, **5**, 6397 (2015).

[36] H. Shirai, N. Akiyama, N. Nunotani, and N. Imanaka, *Chem. Lett.*, **47**, 723 (2018).

[37] R. D. Shannon, *Acta Crystallogr. A*, **32**, 751 (1976).

[38] G. K. Reddy, P. Boolchand, and P. G. Smirniotis, *J. Phys. Chem. C*, **116**, 11019 (2012).

[39] Y. Ji, Z. Zhao, A. Duan, G. Jiang, and J. Liu, *J. Phys. Chem. C*, **113**, 7186 (2009).

[40] L. Yan, T. Ren, X. Wang, D. Ji, and J. Suo, *Appl. Catal. B: Environ.*, **45**, 85 (2003).

[41] R. A. Reimer, C. S. Slaten, M. Seapan, M. W. Lower, and P. E. Tomlinson, *Environ. Prog.*, **13**, 134 (1994).

[42] A. M. Hilmen, D. Schanke, and A. Holmen, *Catal. Lett.*, **38**, 143 (1996).

[43] X.L. Xu and J.Q. Li, *Surf. Sci.*, **605**, 1962 (2011).

Acknowledgments

The author would like to express his heartfelt gratitude to Professor Dr. Nobuhito Imanaka, Department of Applied Chemistry, Graduate School of Engineering, Osaka University, for his continuous guidance, many valuable opinions, and endless support during the course of this work.

The author is very grateful to Dr. Naoyoshi Nunotani of the Department of Applied Chemistry, Graduate School of Engineering, Osaka University, for his excellent guidance and constructive suggestions. The authors are also very thankful to Dr. Shinji Tamura, Department of Applied Chemistry, Graduate School of Engineering, Osaka University, for his stimulating suggestions and discussions in carrying out this work.

The authors would like to express his sincere appreciation to Professor Dr. Shinya Furukawa, Department of Applied Chemistry, Graduate School of Engineering, Osaka University, and Professor Dr. Ken-ichi Nakayama, Department of Applied Chemistry, Graduate School of Engineering, Osaka University, for their valuable and constructive comments during the revision of the thesis.

The author would also thanks to Dr. Hirokazu Izumi (Hyogo Prefectural Institute of Technology) for his assistance with the XPS measurements.

Special thanks should be given to author's co-workers, Dr. Kenji Matsuo, Dr. Hiroaki Shirai, Dr. Yeon-Bin Choi, Mr. Lee Won Joon, Mr. Mizuki Momai, Ms. Yo Shimura, Mr. Okiya Maeda, Mr. Yuki Ogino, Mr. Asuki Sakurai, Mr. Tatsuki Utsunomiya, Ms. Nanako Sanuki, Mr. Yuto Yoshida, Mr. Ryoma Mori, and Mr. Shunsuke Kondo, for their continuous support and helpful assistance during

this work, and also the other members of research group under direction of Professor Dr. Nobuhito Imanaka, Osaka University.

This thesis was financially supported in part by the JST SPRING (grant number JPMJSP2138).

Finally, the author would like to extend his deep gratitude to his parents, Mr. Bao-jun Hu and Ms. Er-ying Chen, his wife, Ms. Hui-min Shen, and all the member of his family for their encouragement, continuous understanding, and perpetual supports.